AGU PUBLICATIONS

JGR

Journal of Geophysical Research: Biogeosciences

RESEARCH ARTICLE
10.1002/2015JG003045

Impact of idealized future stratospheric aerosol injection on the large-scale ocean and land carbon cycles

J. F. Tjiputra[1], A. Grini[2], and H. Lee[1]

[1]Uni Research Climate and Bjerknes Centre for Climate Research, Bergen, Norway, [2]Norwegian Meteorological Institute, Oslo, Norway

Key Points:
- Future idealized large-scale stratospheric aerosol injection (SAI) is simulated using ESM
- The ocean dominates the enhanced carbon sinks leading to a lower atmospheric CO_2 concentration
- SAI is projected to exacerbate the deep ocean acidification

Correspondence to:
J. F. Tjiputra,
jerry.tjiputra@uni.no

Citation:
Tjiputra, J. F., A. Grini, and H. Lee (2016), Impact of idealized future stratospheric aerosol injection on the large-scale ocean and land carbon cycles, *J. Geophys. Res. Biogeosci.*, *121*, 2–27, doi:10.1002/2015JG003045.

Received 5 MAY 2015
Accepted 7 DEC 2015
Accepted article online 14 DEC 2015
Published online 6 JAN 2016

Abstract Using an Earth system model, we simulate stratospheric aerosol injection (SAI) on top of the Representative Concentration Pathways 8.5 future scenario. Our idealized method prescribes aerosol concentration, linearly increasing from 2020 to 2100, and thereafter remaining constant until 2200. In the aggressive scenario, the model projects a cooling trend toward 2100 despite warming that persists in the high latitudes. Following SAI termination in 2100, a rapid global warming of 0.35 K yr^{-1} is simulated in the subsequent 10 years, and the global mean temperature returns to levels close to the reference state, though roughly 0.5 K cooler. In contrast to earlier findings, we show a weak response in the terrestrial carbon sink during SAI implementation in the 21st century, which we attribute to nitrogen limitation. The SAI increases the land carbon uptake in the temperate forest-, grassland-, and shrub-dominated regions. The resultant lower temperatures lead to a reduction in the heterotrophic respiration rate and increase soil carbon retention. Changes in precipitation patterns are key drivers for variability in vegetation carbon. Upon SAI termination, the level of vegetation carbon storage returns to the reference case, whereas the soil carbon remains high. The ocean absorbs nearly 10% more carbon in the geoengineered simulation than in the reference simulation, leading to a ~15 ppm lower atmospheric CO_2 concentration in 2100. The largest enhancement in uptake occurs in the North Atlantic. In both hemispheres' polar regions, SAI delays the sea ice melting and, consequently, export production remains low. In the deep water of North Atlantic, SAI-induced circulation changes accelerate the ocean acidification rate and broaden the affected area.

1. Introduction

Since the preindustrial period, the global carbon cycle has experienced a significant perturbation due to anthropogenic activities. Prior to the industrial revolution, the atmospheric CO_2 concentration was very stable over a millennial time scale [*Etheridge et al.*, 1996], which indicates that the carbon exchanges between the land, ocean, and atmosphere reservoirs were in quasi-equilibrium states (i.e., global source is approximately equal to sink). Today, both the land and ocean combined act as a net carbon sink of roughly 5.3 $\pm$ 1.3 Pg C annually, which reflects more or less half of the anthropogenic carbon emissions from fossil fuel combustion, cement production, and land use change [*Le Quéré et al.*, 2014]. These land and ocean sinks partially offset the ongoing climate change.

Despite the steady increase in carbon uptake by the land and ocean reservoirs, the atmospheric CO_2 concentration has continued to rise at an alarming rate. According to the latest assessment report of the Intergovernmental Panel on Climate Change (IPCC Fifth Assessment Report (AR5)), the accumulated anthropogenic CO_2 in the atmosphere has led to a global increase in surface temperature of 0.85 $\pm$ 0.2 K relative to the preindustrial period [*Intergovernmental Panel on Climate Change (IPCC)*, 2013]. Without any drastic change in the carbon emission trend, the latest climate models project an additional warming of 3.7 $\pm$ 0.7 K under the most pessimistic, business-as-usual-like, future RCP8.5 (Representative Concentration Pathways 8.5) scenario [*Meinshausen et al.*, 2011; *Collins et al.*, 2013]. Even if the anthropogenic carbon emissions are stopped today, global warming will continue for decades to come due to the long lifetime of CO_2 in the atmosphere and the slow ocean response time [*Frölicher et al.*, 2013]. Additionally, other potentially irreversible CO_2-induced climate changes are projected to last for many centuries [*Gillett et al.*, 2011].

As long as the anthropogenic carbon emissions remain unabated, the IPCC-AR5 indicates significant future changes in the Earth system that would lead to unexpected and potentially profound consequences on the society, such as increased vulnerability of water resources, reduced food production yields, increased global

mean thermometric sea level, and an increase in the number of extreme weather events, among others [*IPCC*, 2013]. In addition to climatic impacts, the current rate of surface ocean acidification is unprecedented and its impact on marine ecosystem biodiversity is projected to increase in the future [e.g., *Gehlen et al.*, 2014]. This calls for even greater urgency for concerted international action to combat accelerating, and potentially devastating, climate change. As there is still no global consensus on mitigation through reductions in anthropogenic CO_2 emissions, climate engineering (CE) often arises in climate mitigation and adaptation discussions and is viewed as a potential alternative, or fallback plan, to reduce the most severe impacts of global warming [*IPCC*, 2012].

Climate engineering is defined as a deliberate human-induced large-scale intervention in the climate system to counteract global warming [*Crutzen*, 2006]. It is commonly divided into two groups. The first is represented by activities related to large-scale carbon dioxide removal from the atmosphere, e.g., through enhancing natural carbon sequestration or various methods of direct removal of CO_2 or other greenhouse gases from the ambient atmosphere (including Bio-energy with carbon capture and storage). The second group is related to solar radiation management (SRM) activities, which aim to reduce insolation, e.g., by reflecting a fraction of the incoming solar radiation back to space [*Shepherd*, 2012].

One of the most discussed SRM methods is large-scale stratospheric aerosol injection (SAI), which is often proposed as a possible option to partially offset the anthropogenic radiative forcing [*Robock*, 2013]. However, many practical and technological issues will need to be addressed before the method can be deemed feasible [*Robock et al.*, 2009; *Keith et al.*, 2014]. Past events of explosive volcanic eruptions have been used as a natural analog to SAI. Large volcanic eruptions inject large amounts of different particles and gases into the stratosphere. Among them are sulfur gases, which convert to sulfate aerosols and spread globally with the atmospheric circulation, and these aerosols scatter back part of the incoming solar radiation. The observed radiative effect of this aerosols-induced cloud cover over the next few months to years is a net global cooling [*Robock*, 2013]. Despite the compelling evidence provided by past volcanic eruption events that relatively rapid global cooling can be achieved through increasing the stratospheric aerosol concentration, numerous known and unknown potential negative risks of SAI are still under debate [*Robock et al.*, 2009]. Before any concrete plans or field deployments can be considered, a thorough assessment of SAI effects on the climate system across various spatial and temporal scales is undoubtedly essential. However, it is questionable whether any SAI efforts can be sustained over a long period, and therefore, it is plausible that any future SAI implementations could be abruptly terminated. How the Earth system might respond to such a termination also remains unknown.

In addition to evaluating the feasibility, efficiency, and impact of SAI on the physical climate system, other consequences such as that on the terrestrial and marine carbon cycle and potential feedbacks to climate are still poorly understood. Due to the global nature of SAI, these uncertainties can only be safely studied using the sophisticated Earth system models available today. These models are state-of-the-art and often adopted for the study of large-scale climate variability and projection of future climate change. They are therefore some of the best tools available to study changes in function and interactions of the whole Earth system in response to large-scale global perturbations such as those instigated by climate engineering.

Here we examine potential impacts of SAI on carbon cycle dynamics using the Norwegian Earth System Model (NorESM) with a set of idealized forcings (that mimic SAI) developed to offset the increasing global mean temperature under the RCP8.5 scenario to a cooler climate state (i.e., as in RCP4.5). Specifically, we (i) investigate any potential risks from SAI on the marine ecosystem, particularly pertaining to changes in ocean acidification; (ii) elucidate how changes in ocean circulation and sea ice extent contribute to changes in ocean carbon sink; (iii) identify regional changes in terrestrial carbon sink and storage; and (iv) determine any long-term impact on climate-carbon cycle feedbacks including consequences in response to SAI termination.

Although a number of modeling studies have been dedicated to understanding the impacts of climate engineering on the carbon cycles [e.g., *Matthews and Caldeira*, 2007; *Matthews et al.*, 2009; *Kravitz et al.*, 2013; *Keller et al.*, 2014], they are considerably different to our study. In addition to differences in the simulated climate engineering scenarios, previous studies generally either apply relatively simpler EMIC (Earth system models of intermediate complexity) model frameworks or use ESMs but with a prescribed atmospheric CO_2 concentration and without an interactive carbon cycle. The latter setup, generally based on collection of simulations performed under the GeoMIP (Geoengineering Model Intercomparison Project) [*Kravitz et al.*, 2013]

umbrella, neglects feedbacks arising from land and ocean carbon cycle changes to CO_2 concentration in the atmosphere. Comparisons between our findings with previous studies are provided at the end of the manuscript.

The manuscript is structured as follows. Section 2 describes the model and experimental design. Section 3 presents key results from the model simulations. Section 4 presents additional discussions related to our findings. Finally, concluding remarks are provided in section 5.

2. Methods

2.1. Model Description

In all our model experiments we use the fully coupled Norwegian Earth system model (NorESM1-ME). Here we only briefly describe the key components of the model; for a more detailed description of each component, the reader is referred to *Bentsen et al.* [2013] and *Tjiputra et al.* [2013, and the references therein]. The NorESM1-ME is a state-of-the-art global coupled climate-carbon cycle model. It is based on the Community Climate System model version 4 (CCSM4) developed in the United States [*Gent et al.*, 2011]; therefore, some of the NorESM1-ME components are directly adopted from the CCSM4. For example, the land and sea ice are the same, represented by the Community Land Model version 4 (CLM4) and the Los Alamos National Laboratory sea ice model (CICE4). The atmospheric component is based on the Community Atmospheric Model version 4 (CAM4), with further development at the University of Oslo and the Meteorological Institute of Norway. The CAM4-Oslo differs from the original CAM4 through improvement in the atmospheric chemistry and aerosol-cloud interactions [*Kirkevåg et al.*, 2013]. The ocean component is a coupled biogeochemical ocean general circulation model based on the Hamburg Oceanic Carbon Cycle (HAMOCC5.1) model and the Miami Isopycnic Coordinate Ocean Model. Both the land and atmospheric models have approximately 2° horizontal resolution, whereas the ocean model has 1° with 53 isopycnal layers.

The land carbon cycle module includes carbon-nitrogen coupling; thus, in addition to temperature and precipitation, plant photosynthesis is also limited by the nitrogen availability [*Thornton et al.*, 2009]. Sources and sinks of mineral nitrogen are implemented in the form of atmospheric deposition, biological nitrogen fixation, denitrification, leaching, and losses due to fire events. The plant functional types (PFTs) and land cover change distribution in CLM4 is prescribed and updated annually according to the Coupled Model Intercomparison Project phase 5 (CMIP5) global land use and land cover change data set [*Lawrence et al.*, 2011, 2012]. The transient PFT and land cover fields take into account historical and future climate change under RCP8.5 scenario (1850–2100), which were derived using the global land model and Integrated Assessment Model, respectively. Details on PFT and land cover implementation in the CLM4 model are described in *Lawrence et al.* [2012].

The HAMOCC5.1 model is based on the original work by *Maier-Reimer* [1993], and it was further improved in *Maier-Reimer et al.* [2005]. The version used here includes a standardized inorganic seawater carbon chemistry following the Ocean Carbon-Cycle Model Intercomparison Project protocols. HAMOCC5.1 includes a nutrient-phytoplankton-zooplankton-detritus-type ecosystem module in the euphotic layer. Biological productivity (i.e., phytoplankton growth rate) is colimited by light, temperature, and nutrients such as phosphate, nitrate, and dissolved iron [*Six and Maier-Reimer*, 1996; *Assmann et al.*, 2010]. Air-sea exchange of CO_2 and O_2 gases are prognostically simulated as a function of atmospheric concentration, wind speed, and surface ocean physical and biogeochemical properties.

The NorESM1-ME contributed to the IPCC-AR5 and CMIP5 (Coupled Model Intercomparison Project phase 5) [*Taylor et al.*, 2012]. Its performance and projections of the ocean biogeochemical response to climate change have been assessed and documented in multiple publications [e.g., *Bopp et al.*, 2013; *C. Jones et al.*, 2013; *Hoffman et al.*, 2014].

2.2. Experimental Setup

Prior to the sensitivity experiments, the NorESM1-ME was spun up fully coupled for more than 1000 model years at preindustrial boundary conditions. Within the last 100 years, the model is in a reasonably steady state, with the global mean atmospheric CO_2 concentration fluctuating between 282 and 286 ppm. Next, the following standard reference runs (i.e., without SAI forcing) were performed: historical (hist), future RCP4.5 (r45),

Table 1. List of the Performed Model Experiments

Name	Description	Period (Year)	SAI Forcing
hist	Historical	1850–2005	None
r45	RCP4.5	2006–2100	None
r85	RCP8.5	2006–2200	None
r85ce1	RCP8.5 with CE1	2006–2100	Linearized up to 2 times Pinatubo (2020–2100)
r85ce2	RCP8.5 with CE2	2006–2200	Linearized up to 5 times Pinatubo (2020–2100) and kept constant at 5 times Pinatubo (2101–2200)
r85ce2t	r85ce2 with termination	2101–2200	Branch out from r85ce2 but without CE

and RCP8.5 (r85), as described in Table 1. Table 1 also depicts the integration periods for each experiment. These simulations apply the standard forcing and boundary conditions following the CMIP5 protocol [*Taylor et al.*, 2012].

To simulate an artificial climate engineering scheme, we implemented a linearly increased stratospheric mass mixing ratio of SO_4, scaled to the observed monthly spatial distribution of SO_4 in the year following Mount Pinatubo eruption in 1991 (i.e., September 1991 to August 1992). The forcing was designed to imitate an idealized SAI-based climate engineering. The Pinatubo eruption occurred in the tropics, resulting in maximum aerosol concentrations in the low latitudes during the first few months following the event (October 1991). Figure 1a shows that as the aerosol concentration decreases in the low latitudes, by April 1992, it had spread poleward and reached the high latitudes of both hemispheres.

The NorESM1-ME uses the data set created by *Ammann et al.* [2003] to describe the historical evolution of volcanic forcing. In this study, we have chosen the year directly following the Pinatubo eruption in 1991 in the data set and defined that aerosol content as "1xPinatubo." When creating scenarios for SAI, we assumed that

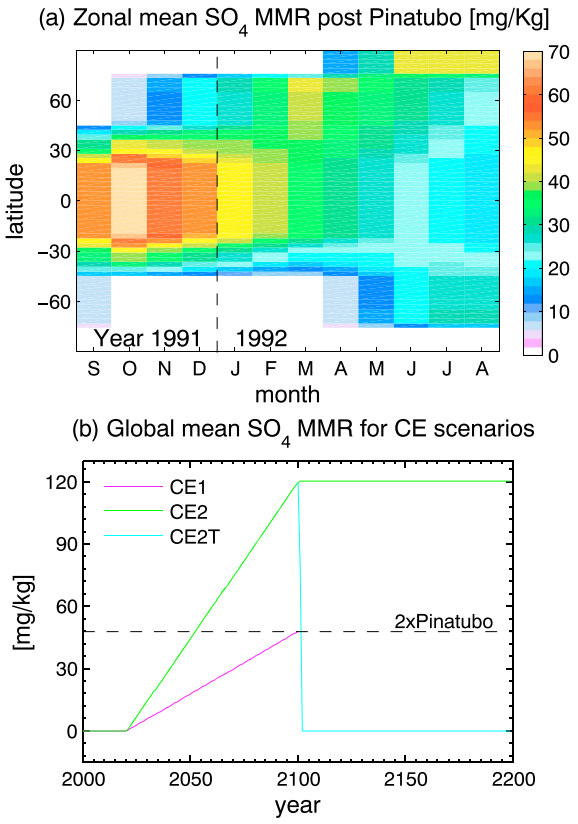

Figure 1. (a) Hovmöller diagram of zonal mean of SO_4 mass mixing ratio concentration following Mount Pinatubo eruption from September 1991 to August 1992 and (b) time series of global mean of SO_4 concentration for the CE1, CE2, and CE2T forcings to mimic future stratospheric aerosol injection scenarios (see also text and Table 1).

we could scale this aerosol content to any concentration levels needed to counteract the greenhouse gas forcing of RCP8.5. The scaled aerosol concentration from the typical Pinatubo year, including its yearly cycle, is then repeated in the model during the period of climate engineering. Using a constant scale factor, the aerosol concentration in a specific year is linearly scaled relative to the previous year. This method allows us to create a forcing data set from x times Pinatubo in year $t1$ to y times Pinatubo in year $t2$, where x, y, $t1$, and $t2$ can be arbitrarily selected. The method is desirable as it allows us to estimate how much SAI forcing is required in terms of the Mount Pinatubo eruption magnitude.

We note that this method ignores the evolution of particle sizes, an important aspect of SAI. As aerosol concentrations increase, coagulation increases leading to larger particle sizes, and this leads to less efficient scattering of short-wave radiation [*Niemeier et al.*, 2011]. Though the aerosol becomes a less efficient scatterer, an increase in the emissions is still expected to increase the reflected amount of solar radiation. This applies at least to levels where the stratospheric aerosols can provide the expected net radiative imbalance, e.g., the -4 W m^{-2} difference between the RCP8.5 and RCP4.5 in the year 2100 [*Tilmes et al.*, 2015]. *Niemeier and Timmreck* [2015] found that SAI could provide 8 W m^{-2} of forcing for approximately 80 Tg S yr^{-1}. In our study, we used a scaling factor of 5 times Pinatubo to get the same effect (8.5 W m^{-2} would be needed to cancel out RCP8.5 radiative forcing). This seems reasonable given that the emissions from the Pinatubo eruptions were approximately 10 Tg S, and in our scaling procedure we did not take into account changes in particle size or the aerosol effect on the long-wave radiation and climate feedbacks due to interactions with ozone.

For simplicity, our method also replicates the spatial and temporal pattern of the stratospheric aerosol concentration observed following the Pinatubo eruption. Such a pattern may not be optimal and is likely to be different to the aerosol-cloud distribution from a more realistic forcing [e.g., *Ferraro et al.*, 2014; *Tilmes et al.*, 2015]. Different aerosol distributions could have impact on regional climate responses, and consequently the carbon cycle (see also section 4).

We developed two linearly increased SAI scenarios that begin in year 2020 to 2100 (September 2021 to August 2101). The first scenario (CE1) is based on linear scaling from 0 times Pinatubo at 2020 up to 2 times Pinatubo by the year 2100, and the second scenario (CE2) is up to 5 times Pinatubo, as illustrated in Figure 1b. CE1 forcing was implemented and targeted at bringing the projected global mean surface temperature under the RCP8.5 down to a level close to the RCP4.5 scenario by the end of the 21st century. The stronger CE2 forcing was introduced mainly to assess the impact of an aggressive future SAI scenario on the global carbon cycle. The CE2 forcing scenario is continued to 2200 while maintaining 5 times Pinatubo forcing in the 22nd century.

All experiments were performed with the fully interactive carbon cycle based on prescribed anthropogenic CO_2 emissions, not with prescribed concentrations. This configuration allows for a prognostic regionally varying atmospheric CO_2 concentration taking into account the CO_2 fluxes across the air-sea and air-land interfaces, hence allowing a direct climate-carbon cycle feedback to be simulated. The annual prescribed anthropogenic CO_2 emissions due to fossil fuel burning and land use change for the historical and future RCP4.5 and RCP8.5 scenarios are shown in Figure 2a. Under RCP4.5, fossil fuel emissions peak at roughly 11 Pg C yr^{-1} around the 2040s and decline thereafter. Under RCP8.5, the fossil fuel emissions increase faster to a maximum of 28.5 Pg C yr^{-1} by the end of the 21st century. For experiments beyond the year 2100 (only under the RCP8.5 scenario), we applied repeated prescribed land use change, ozone concentration, aerosol deposition, and atmospheric greenhouse gases boundary conditions taken from the year 2100. The CO_2 emissions remain at 2100 emission level after 2100, before linearly declining from 2150 onward. Except for the land use change, the extended RCP8.5 scenario follows the Extended Concentration Pathway 8.5 as described in *Meinshausen et al.* [2011].

In order to assess future changes in the global carbon budget between intermediate mitigation scenario RCP4.5 versus nonmitigated RCP8.5 but with climate engineering, we performed simulation "r85ce1" where the CE1 forcing is added on top of the RCP8.5 scenario up to the end of the 21st century. A second simulation with stronger forcing CE2 on top of the RCP8.5 scenario, "r85ce2," was also performed. Since we find a relatively weak response of the land and ocean biogeochemistry to the CE1 forcing, we focus our analysis with respect to carbon cycle impacts on the r85ce2 simulation results. Lastly, additional simulation is branched from r85ce2 to examine the effect of SAI termination from 2101 to 2200 (r85ce2t). These experiments are summarized in Table 1.

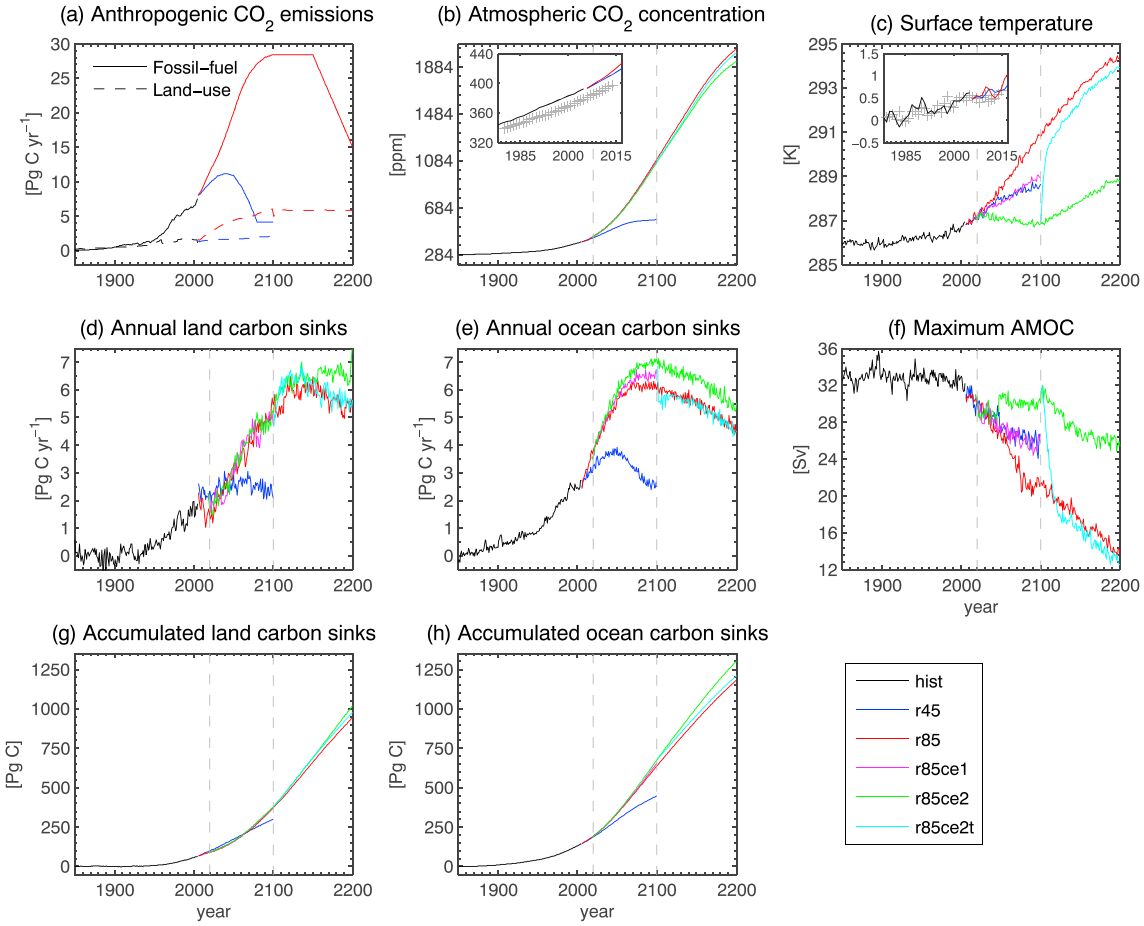

Figure 2. Time series of projected (a) annual anthropogenic CO_2 emissions, (b) atmospheric CO_2 concentration, (c) global mean surface air temperature, (d) annual land carbon sink (5 year running mean), (e) annual ocean carbon sink, (f) maximum Atlantic Meridional Overturning Circulation (AMOC), (g) accumulated land carbon sink, and (h) accumulated ocean carbon sink for each simulation listed in Table 1. Dashed grey lines represent the beginning and end periods of linear increase of climate engineering forcing. Inset in Figure 2b represents values for the 1980–2015 periods with the observed global mean atmospheric CO_2 (plus symbol) [*Conway et al.*, 1994]. Inset in Figure 2c represents anomalies (relative to 1961–1990) of mean surface temperature with the observation from HadCRUT4 [*Kennedy et al.*, 2011].

3. Results

Under the RCP8.5 scenario (r85), the net top of the atmosphere (ToA) radiative imbalance increases from approximately 1 W m^{-2} in 2020 to roughly 3 W m^{-2} by 2100 (Figure 3, left). Under the weaker SAI scenario (r85ce1), this increase is dampened, leading to 2 W m^{-2} at the end of this century. This is comparable to the respective radiative balance simulated under the RCP4.5 scenario. In the stronger SAI scenario (r85ce2), the trend is reversed, reducing the ToA radiative balance to about 0.5 W m^{-2} in 2100.

Next, we analyze how SAI alters the radiative components within the atmospheric column. For this, we compute the mean changes (r85ce2 compared to r85) in short-wave (SW), long-wave (LW), latent heat, and sensible heat fluxes for the 2060–2069 period, which approximately represents the middle of SAI implementation, as shown in Figure 3 (right). It shows that CE results in lower net downward SW and net upward LW fluxes at the ToA by 8.5 W m^{-2} and 6.6 W m^{-2}, respectively. This leads to a net cooling of roughly 2 W m^{-2}. There is a large difference in the long-wave flux going from the atmosphere to the surface. In the cooler r85ce2 simulation, the atmosphere sends 14 W m^{-2} less long-wave toward the surface.

At the surface, the r85ce2 climate receives 6 W m^{-2} less energy from SW radiation than the reference r85 simulation. Since the LW energy flux from the atmosphere is much smaller, the surface in r85ce2 cools further (2.6 W m^{-2}) compared to r85. This net surface influx reduction of 8.6 W m^{-2} is compensated by less latent (6.4 W m^{-2}) and sensible (0.4 W m^{-2}) heat releases and less heat uptake by the ocean (1.8 W m^{-2}).

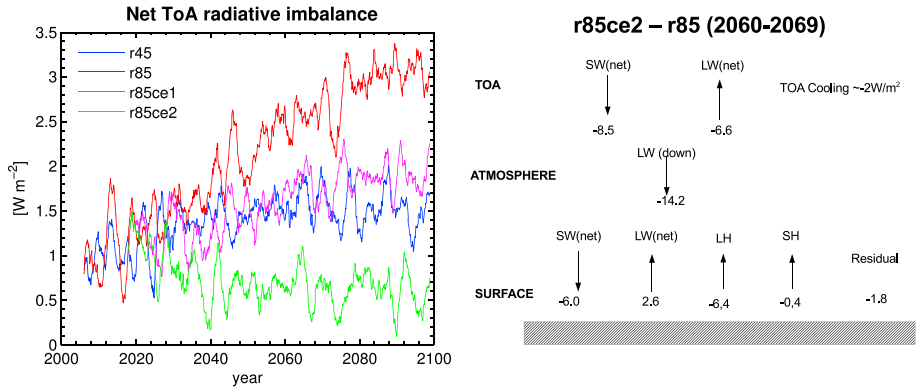

Figure 3. (left) Monthly time series of net top of the atmosphere (ToA) radiative imbalance simulated in each simulation for the 2006–2100 period. Shown here are 24 months running mean values. (right) Schematic diagram of mean changes (r85ce2 minus r85) in radiative balance properties at ToA, atmosphere, and surface for the 2060s period.

Note that all numbers represent transient net fluxes during the 2060–2069 period computed from a coupled model simulation. The fluxes, therefore, include feedback mechanisms and do not represent estimates of equilibrium radiative forcing. The latter can be estimated by applying model simulations with fixed ocean temperature.

3.1. Projected Atmospheric CO_2 and Surface Temperature

The model simulations start from the preindustrial climate (Table 1) in year 1850 with an atmospheric CO_2 concentration of 284 ppm. By the end of the historical period (year 2005), the atmospheric CO_2 has increased to 393 ppm, slightly higher than the observational estimate of 379 ppm (www.esrl.noaa.gov/gmd/ccgg/trends/). By 2100, the atmospheric CO_2 increases to 583 and 1097 ppm for simulations r45 and r85, respectively, as shown in Figure 2b. For the SAI scenarios, the projected atmospheric CO_2 only decreases slightly to 1085 and 1072 ppm by 2100 in r85ce1 and r85ce2, respectively (see also Table 2). These reductions reflect an additional combined net carbon sink by the land and ocean reservoirs. By the end of the 22nd century the atmospheric CO_2 concentration in r85ce2 continues to diverge (1930 ppm) relative to r85 (2035 ppm). When the SAI is terminated (in r85ce2t), the atmospheric CO_2 slightly rebounds toward the baseline case (to 2005 ppm by 2200).

The impact of SAI on the simulated global mean surface temperature is very pronounced (Figure 2c). For r85ce1, the model projects a weaker surface temperature increase than in r85 of nearly 2 K by 2100 and is comparable to that of the RCP4.5 scenario. Under r85ce2, the model projects global net cooling with surface temperatures in 2100 comparable to the present-day condition (~4 K lower than r85 at 2100). In the 22nd century, the constant SAI forcing under r85ce2 maintains a cooler temperature relative to r85, though the temperature starts to climb again after SAI is held constant in 2100.

Despite similarity in the projected global mean surface temperature between r45 and r85ce1, the simulations show distinct spatial features. Figure 4 shows that for most of the low-latitude regions, the surface warming simulated under the RCP8.5 scenario can be suppressed with SAI (see Figures 4a and 4c), yielding similar

Table 2. Global Mean Values for Key Climate Metrics for the Preindustrial (1850) and Projected in the Future (2100 and 2200) for Each Simulation

	pi	r45	r85		r85ce1	r85ce2		r85ce2t
Fields	1850	2100	2100	2200	2100	2100	2200	2200
Surface temperature (K)	285.88	288.66	290.83	294.36	288.95	287.06	288.81	293.93
Precipitation (mm d $^{-1}$)	2.78	2.91	3.01	3.19	2.80	2.58	2.65	3.16
Atmospheric CO_2 (ppm)	284.22	583.01	1086.66	2034.74	1085.31	1071.62	1929.55	2004.91
Arctic sea ice area (10^6 km^2)	11.30	7.46	4.32	0.16	6.95	9.51	6.40	0.26
Antarctic sea ice area (10^6 km^2)	14.28	11.54	9.04	1.04	9.87	11.64	8.79	2.43
Surface pH (pH unit)	8.15	7.90	7.66	7.41	7.66	7.67	7.43	7.42
Oxygen content (Pmol O_2)	340.13	339.90	336.59	320.62	338.93	341.96	336.67	324.66

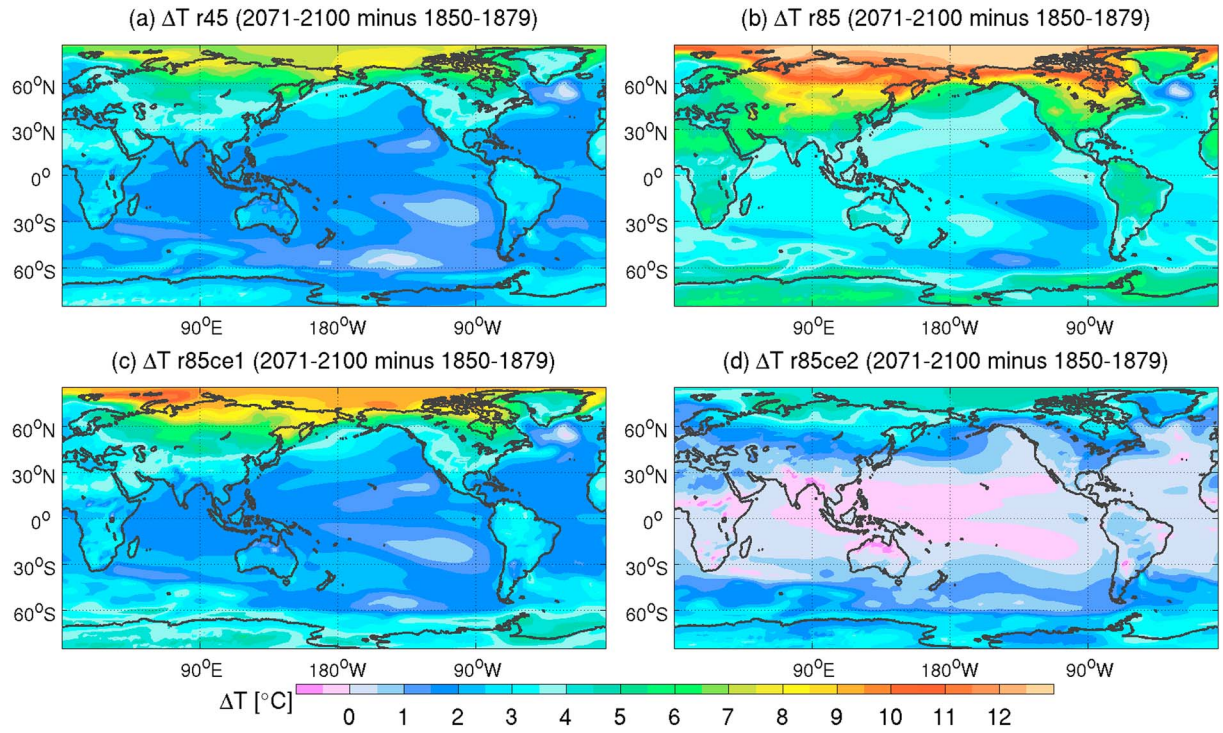

Figure 4. Maps of changes in surface air temperature by the end of the 21st century (2071–2100) relative to the preindustrial period (1850–1879) as simulated under simulations (a) r45, (b) r85, (c) r85ce1, and (d) r85ce2.

spatial warming patterns as those simulated under the RCP4.5 scenario. However, in high-latitude regions (poleward of 60°), substantial warming of roughly 5 K and 10 K, respectively, is still projected in both Southern and Northern hemispheres relative to the preindustrial condition. Under r85ce2, the majority of the tropical Pacific and Indian Oceans have surface air temperature close to, or lower than, the preindustrial state. At high latitudes a maximum warming of approximately 5 K is still simulated in the Arctic Ocean.

Following SAI termination, the model projects rapid global warming of roughly 3.5 K over the next 10 years. This rapid warming roughly brings the global climate back close to the non-SAI warmer state. Thereafter, the warming trend follows the reference r85 simulation trend (Figure 2c) toward the end of the 22nd century. The r85ce2t experiment indicates that once terminated, SAI could still induce long-lasting minor but potentially detectable effects on the global mean surface temperature. Here the projected global mean temperature by the year 2200 for the r85ce2t simulation remains about 0.5 K lower than the non-SAI simulation r85. Conversely, if SAI is continued, the global temperature will be roughly 5.6 K colder.

Figure 2f shows that SAI also impacts the projected large-scale ocean overturning circulation. Depending on the magnitude of SAI forcing, the reduction of the Atlantic Meridional Overturning Circulation (AMOC) due to climate change can be alleviated or even reversed. Once SAI ceases, the AMOC immediately reverts toward the

Table 3. Cumulative Land and Ocean Carbon Sinks for the 2020–2100 and 2101–2200 Periods in (Pg C) From Each Future Scenario Simulation

	Land		Ocean	
Experiments	2020–2100	2101–2200	2020–2100	2101–2200
r45	201.84	-	263.61	-
r85	282.23	572.50	449.33	543.68
r85ce1	284.24	-	466.77	-
r85ce2	288.29	641.52	487.85	626.75
r85ce2t	-	598.13	-	533.57

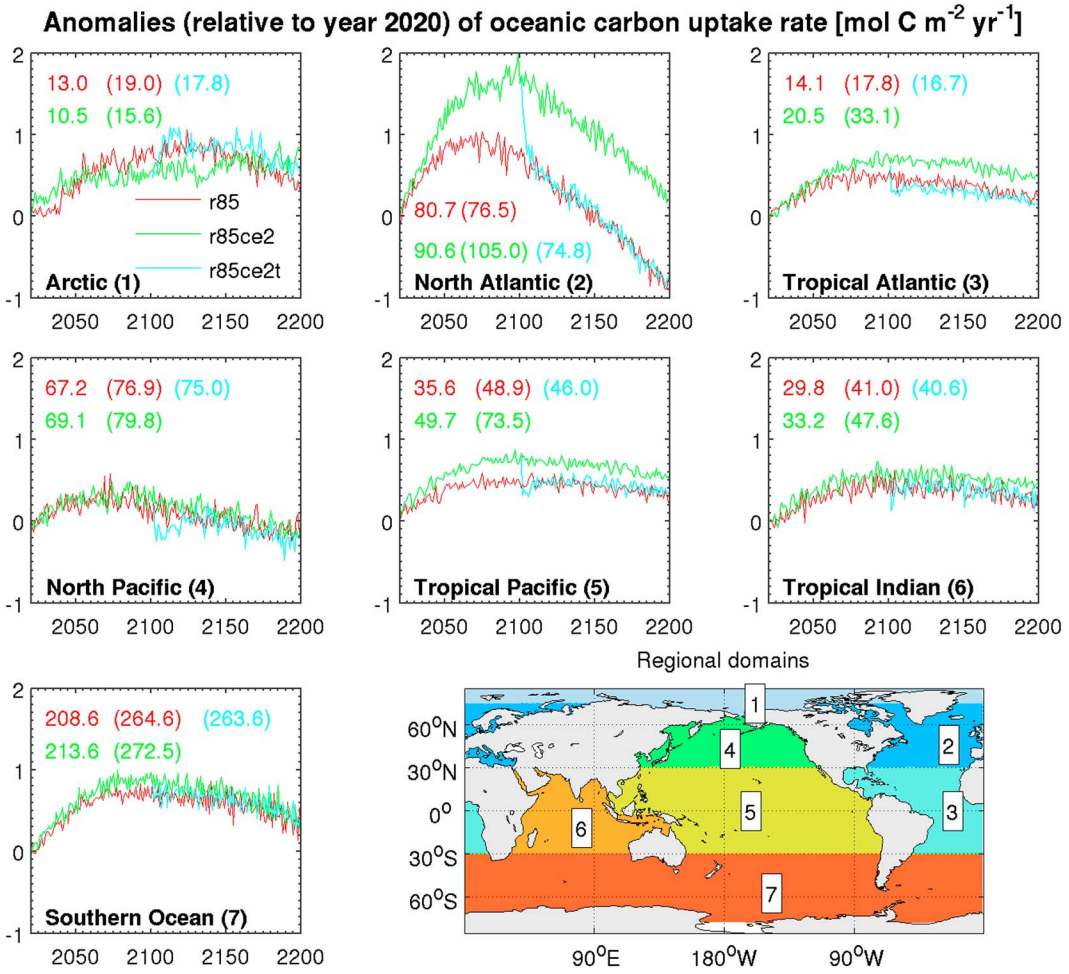

Figure 5. Time series of carbon uptake strength anomalies (relative to year 2020) in seven ocean regions for the period 2020–2200 as simulated by simulations r85 (red lines) and r85ce2 (green lines), and for the 2101–2200 period for the r85ce2t (cyan lines) in (mol C m^{-2} yr^{-1}) units. The number outside (inside) the parentheses represent the absolute cumulated carbon sinks for the 2020–2100 (2101–2200) period in Pg C unit. Regional domains are defined according to ocean basins and 30° latitude lines, as shown in the lower right map.

reference r85 state over the next 10 years and eventually becomes slightly weaker thereafter. Other changes in key climate metrics such as global mean precipitation and sea ice areas simulated in the years 2100 and 2200 for each experiment are listed in Table 2.

3.2. Changes in Oceanic Carbon Sink

Figure 2e shows that the ocean takes up more carbon when SAI forcings are included in both r85ce1 and r85ce2 relative to the reference simulations. Cumulatively, Table 3 shows that the ocean takes up 17.4 Pg C more in r85ce1 than in r85 (449.3 Pg C) between 2020 and 2100. Under the aggressive SAI scenario, the global ocean sequesters almost 10% (i.e., 38.5 Pg C) more carbon for the same period. In order to analyze the regional variability in the ocean carbon uptake, we divided the world ocean into seven domains according to the ocean basins and 30° latitudinal lines, as illustrated in Figure 5.

As expected, following the higher atmospheric CO_2 concentration, the projected ocean uptake rate under the reference scenario (r85) increases relative to the present-day before it stabilizes toward the end of the 21st century in all regions, except for the Arctic and North Atlantic (red lines in Figure 5). In the Arctic the uptake rate steadily increases, whereas in the North Atlantic it starts to decline in the 2070s. When SAI is included (r85ce2), the uptake strength generally increases in all regions, except for the Arctic Ocean. The largest enhancement occurs in the North Atlantic, where the uptake rate anomaly increases by more than 1 mol C m^{-2} yr^{-1} by the end of the 21st century. Other regions with a substantial increase in carbon sink anomalies are the tropical Pacific and tropical Atlantic regions. In the Arctic, as shown in Figure 5, SAI implementation somewhat reduces

the carbon sink in the second half of the 21st century. We attribute this to the larger sea ice extent, which blocks and limits the air-sea gas exchange in r85ce2. In the Southern Ocean, despite representing 30% of the world ocean area, the cumulative carbon sink only increases by 5 Pg C (or 13% of the total global difference between r85 and r85ce2) for the 2020–2100 period. In contrast, the North Atlantic represents only 7% of the world ocean area, but here the cumulative carbon uptake increases by nearly 10 Pg C or 26% of the additional global carbon sink for the same period. In the 22nd century, the model projects a declining trend in ocean carbon uptake rate in all regions. This feature is attributed to the decreasing oceanic CO_2 buffering capacity (i.e., the ability to dissociate dissolved CO_2 into other dissolved inorganic carbon compounds) at higher ambient CO_2 levels [*Heinze et al.*, 2015]. In addition, higher sea surface temperature (SST) and slowdown in ocean circulation are expected to lower the CO_2 solubility in seawater and reduce the carbon sequestration efficiency. *Tjiputra et al.* [2014] also show that a decline in atmospheric CO_2 growth rate (e.g., in the 22nd century) will also reduce the oceanic carbon uptake rate.

Changes in ocean carbon sink are largely driven by the disequilibrium state between the atmospheric and surface ocean partial pressures of CO_2. The latter depends predominantly by the concentration of surface dissolved inorganic carbon (DIC), which is regulated by two key mechanisms: the solubility and biological pumps [*Volk and Hoffert*, 1985]. The solubility pump is governed by the physical properties of the ocean such as temperature and circulation, which determine how much carbon can be dissolved and transported from the surface to the ocean interior, whereas the biological pump creates a vertical gradient in DIC through gravitational sinking and remineralization of particulate organic carbon at depth. In the model, the biological pump can partly be estimated from the export of particulate organic carbon out of the euphotic zone at 100 m depth (i.e., export production). We note that a change in the export production alone is not a direct representation of the biological carbon pump change, due to the large spatial variations in the efficiency of biological-mediated carbon sequestration [*DeVries et al.*, 2012]. Here the export production analysis is shown to illustrate how changes in biological production due to SAI forcing could be related to the simulated changes in the air-sea carbon flux. For most of the ocean regions, except for the Arctic and the Southern Ocean, changes in oceanic carbon sinks during SAI implementation to some extent resemble the changes in the respective regional export production.

Figure 6a shows that SAI-induced increases in carbon uptake in the North Atlantic, North Pacific, and the Southern Ocean occur predominantly during the summer season of the respective hemispheres (i.e., June-July-August (JJA) and December-January-February (DJF) months). In the same season, the model also simulates a comparable increase in export production (Figure 6d). Increases in export production can be explained by changes in nutrient supply into the surface by mixing and upwelling processes [*Steinacher et al.*, 2010]. Under the baseline r85 simulation, the future surface productivity is projected to decline due to lower nutrient upwelling from stronger stratification. SAI alleviates this effect in r85ce2 where the model is able to maintain the biological productivity rate at the 2020 level (not shown). In the North Pacific, the export production during spring (March-April-May (MAM)) period in r85 is projected to increase, whereas it stabilizes in r85ce2. Here the biological production during spring is limited by both temperature and light [see also *Bopp et al.*, 2013]. The temperature limitation is ameliorated with SST warming, but this is not the case when SAI is included. In the North Atlantic, the total change in export production explains only about 25% of the carbon sink increase. This suggests that the SAI-induced changes in physical processes could play a bigger role in this region. This is consistent with the AMOC decrease in the r85 simulation. The cooler climate in r85ce2 maintains the relatively strong AMOC allowing for a more efficient pathway for transporting dissolved inorganic carbon into the interior.

In the tropical Pacific, Atlantic, and Indian Oceans, SAI also alleviates the reduction in export production throughout the 2020–2100 period with magnitudes that are comparable to the net increase in carbon sinks within the respective regions in r85ce2 relative to the r85 simulations. In the Southern Ocean, SAI induces higher cumulative export production in the summer (DJF) of 7.1 Pg C, as also seen in the respective carbon uptake (7.4 Pg C). Here reduction in the ocean carbon uptake during winter and spring (JJA and SON) in r85ce2 could be attributed to changes in the surface wind speed. Under future climate change, it has been shown that the Southern Annular Mode would shift poleward and intensify. The associated strengthening of surface wind stress has been projected to increase the anthropogenic CO_2 sink in this region due to more efficient subduction and northward transport of the intermediate water masses containing anthropogenic carbon [see also *Lovenduski and Ito*, 2009; *Tjiputra et al.*, 2010]. This mechanism is suppressed in r85ce2 simulation.

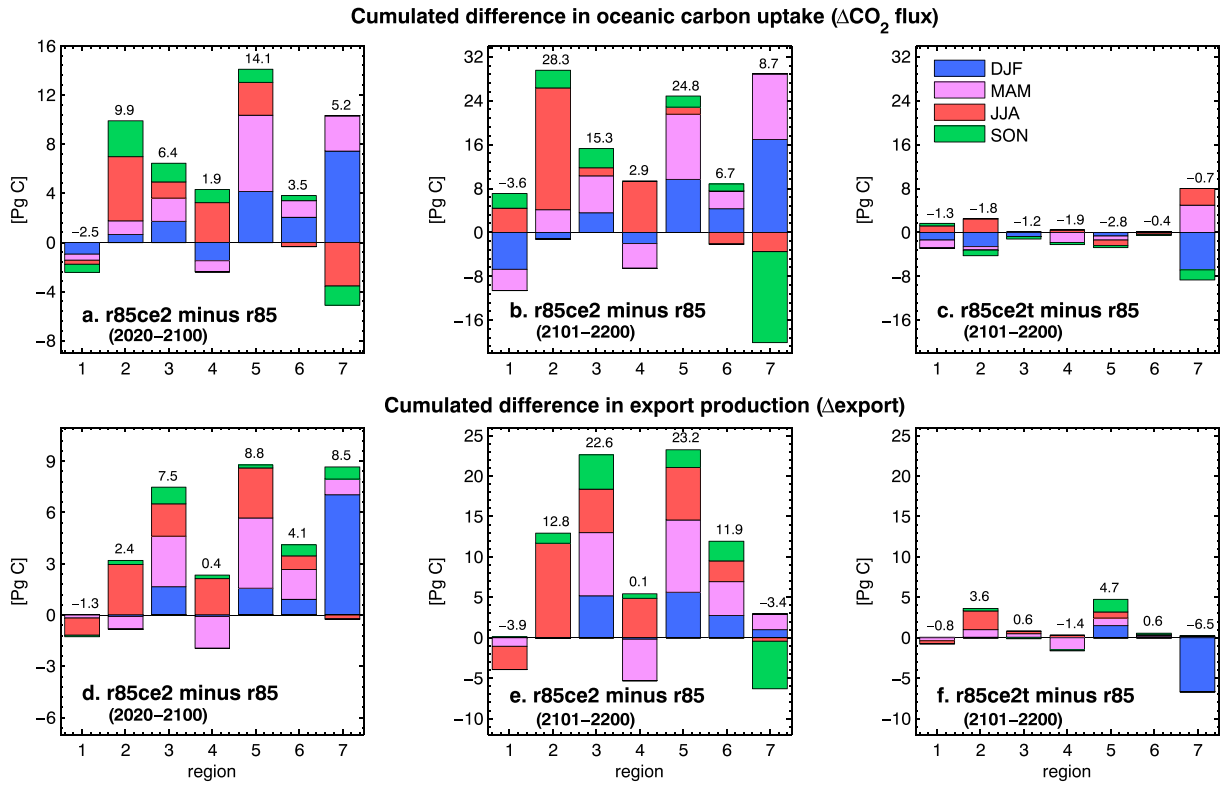

Figure 6. Cumulated differences between simulations r85ce2 and r85ce2t with the baseline r85 in (a–c) oceanic carbon uptake and (d–f) export production at 100 m depth, distinguished by the four seasons of DJF (December-January-February), MAM (March-April-May), JJA (June-July-August), and SON (September-October-November). The numbers on top of each bar denote the total of all seasons. Shown here are integrated values for 2020–2100 (Figures 6a and 6d) and 2101–2200 (Figures 6b, 6c, 6e, and 6f) periods. The region number on the *x* axis is according to Figure 5.

In the period following SAI termination (2101–2200), Table 3 shows that there is a considerable decrease in the ocean carbon uptake (r85ce2t) compared to the case if SAI implementation is continued (r85ce2) and a slight decrease compared to the reference r85 simulation (see also Figure 2). Regionally, the same feature is also illustrated in Figure 5 (cyan lines). After the SAI cessation, the carbon uptake rate is immediately reduced to that projected in r85. In the middle- and low-latitude regions, this decrease is related to the rapid SST warming, which reduces the CO_2 gas solubility in seawater following the SAI termination (not shown). This suggests that the SAI-induced impact on the ocean carbon uptake is not long lasting and is reversible relatively rapidly. The regress is also true for the North Atlantic region, where the largest decrease in uptake strength is projected once SAI is terminated, with a cumulative carbon uptake (2101–2200) nearly 2 Pg C lower in r85ce2t than in r85. In the Southern Ocean, a considerable increase in carbon uptake is simulated in the fall and winter but is further offset by the decrease in the spring and summer (see Figure 6c).

For the 2101–2200 period, if SAI is continued, the model still projects higher export production in nearly all regions, except for the high latitudes. If SAI is discontinued, there is less change in the cumulative export production, except for the North Atlantic, tropical Pacific, and the Southern Ocean (Figure 6f). In the North Atlantic, the projected post-SAI export production (r85ce2t) in the spring and summer also declines toward the end of the 22nd century, although it remains higher than r85 (not shown), accounting for approximately 3 Pg C higher cumulative export production. In the tropical Pacific, higher export production predominantly occurs in the transition period, i.e., the first 20–30 years following SAI termination.

In the Southern Ocean, higher summer surface productivity in the 21st century occurs in r85ce2 compared to r85 because SAI-induced cooling inhibits stronger stratification. In the 22nd century the opposite occurs, i.e., the productivity in both r85ce2 and r85ce2t simulations are lower than the baseline simulation r85 (see also Figures 6e and 6f). Regionally, the lower export production is most apparent along the Antarctic sea ice edges, associated with the timing of the sea ice retreat (Figure 7). In both the r85 and r85ce2 simulations, the sea ice is projected to steadily decline, with slightly faster rate in the former. However, in the second half

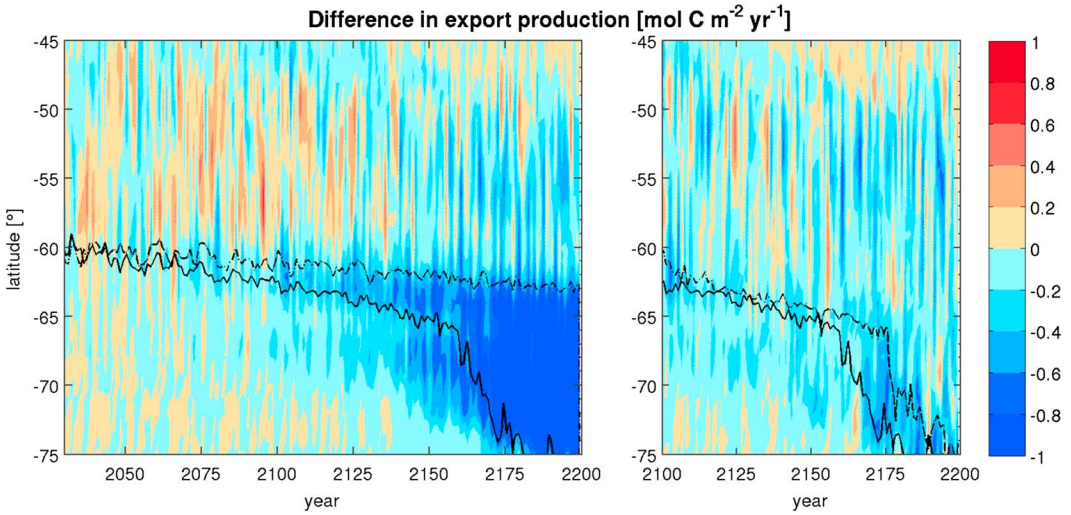

Figure 7. Hovmöller diagram of difference in zonally averaged December ocean export production (left) for r85ce2 minus r85 for the 2020–2200 period and (right) for r85ce2t minus r85 for the 2101–2200 period. Solid (dashed) line represent the latitude where the mean sea ice coverage is 20% for the r85 (r85ce2 and r85ce2t) simulation.

of the 22nd century, a rather rapid decline in sea ice extent is simulated between the years 2160 and 2180 in r85, leading to a nearly ice free summer. This feature reduces the temperature limitation for surface biological productivity. With warmer SSTs, the phytoplankton growth rate in r85 is higher than in r85ce2 and r85ce2t and subsequently results in higher export production. Figure 7 also shows that in r85ce2, this rapid sea ice decline is not simulated and in r85ce2t delayed by approximately 20 years.

In order to qualitatively delineate the role of different physical and chemical drivers in enhancing the regional carbon sinks, we computed the term $\partial C_T/\partial pCO_2$, which measures the change in total dissolved inorganic carbon in the seawater for a small perturbation in surface ocean partial pressure of CO_2. In CO_2 uptake (outgassing) regions, a high value of $\partial C_T/\partial pCO_2$ corresponds to higher uptake (outgassing) rate than regions with low $\partial C_T/\partial pCO_2$ for a given small change in atmospheric pCO_2. A low value indicates the opposite. The equilibrium calculation is computed, using seawater carbon system software CO2SYSv1.0 released by the Carbon Dioxide Information Analysis Center [*Lewis and Wallace*, 1998] applying dissociation constants of *Mehrbach et al.* [1973] as refitted by *Dickson and Millero* [1987], as follows:

$$\frac{\partial[C_T]}{\partial[pCO_2]} = \frac{[C_T]}{\mathrm{RF} \times [pCO_2]} \tag{1}$$

where RF, pCO_2, and C_T represent the Revelle factor [*Revelle and Suess*, 1957], surface ocean partial pressure of CO_2, and total concentration of dissolved inorganic carbon, respectively. First, we calculated equation (1) using mean values simulated in the North Atlantic region for all seasons using the area-weighted regional mean from both r85 and r85ce2 simulations. To illustrate the sensitivity of $\partial C_T/\partial pCO_2$ to changes in SST (sea surface temperature), we compute equation (1) for a typical range of SST in the North Atlantic, while keeping the sea surface salinity (SSS), DIC, and alkalinity constant (Figure 8a). We repeat the calculation for sensitivity to SSS, DIC, and alkalinity, as shown in Figures 8b–8d for all seasons (DJF, MAM, JJA, and SON). We use the SST, SSS, DIC, and alkalinity values from the 2071 to 2100 period, when the SAI effect over the 21st century is expected to be largest between the two experiments.

In the North Atlantic, Figure 8a shows that SST simulated in r85ce2 is always colder than in r85, leading to higher $\partial C_T/\partial pCO_2$ values. This indicates a higher carbon uptake efficiency in r85ce2 than r85 when considering SST change alone. Figure 8b shows very little sensitivity (i.e., increase) in $\partial C_T/\partial pCO_2$ to changes in SSS. The mean surface DIC is always lower in r85ce2 than in r85, which could be attributed to the more efficient export of surface DIC to depth in r85ce2 through stronger AMOC and higher export production (see also Figure 6d). As with SST, lower DIC corresponds to higher carbon uptake efficiency in r85ce2. The alkalinity in r85ce2 is also lower than in r85, but it has the opposite effect on $\partial C_T/\partial pCO_2$. The difference in surface alkalinity between the two experiments closely resembles that of the surface salinity (Figures 8b and 8d), suggesting a dominant influence of changes in precipitation and evaporation patterns. Consistent with earlier studies,

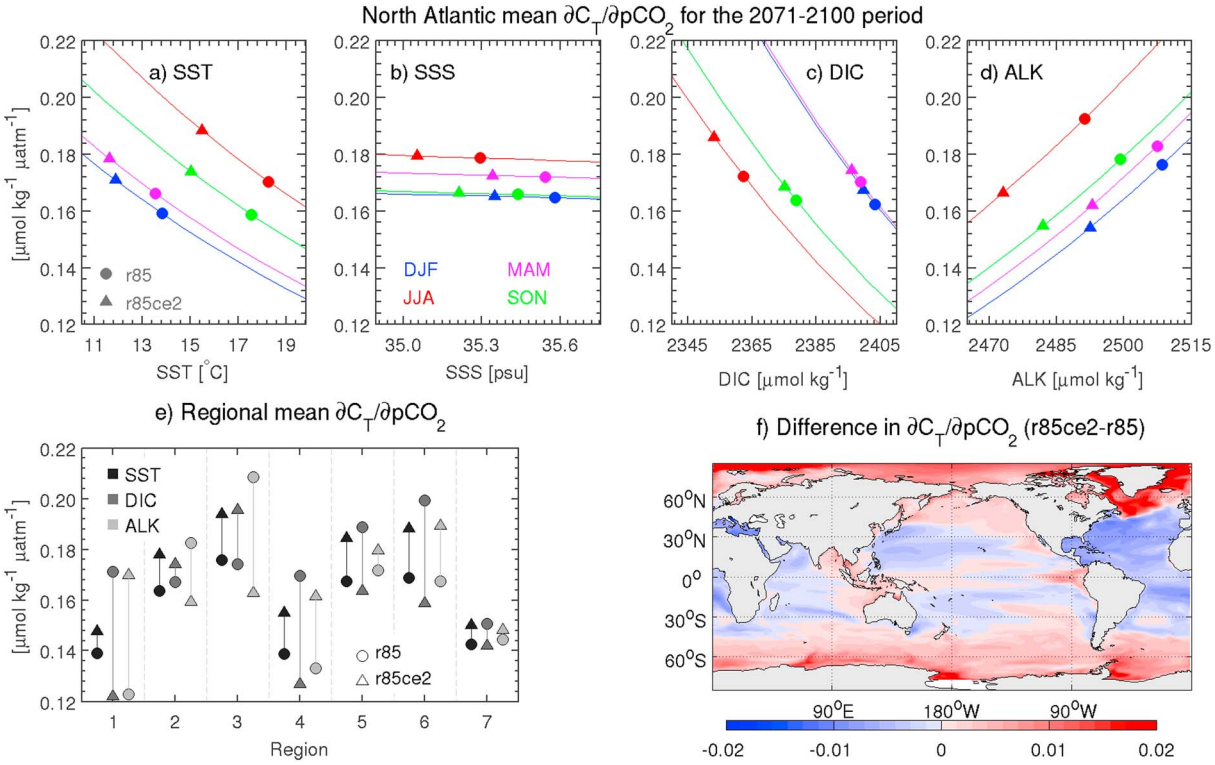

Figure 8. Rate of change of total carbon (C_T) to change in surface pCO_2 ($\partial C_T/\partial pCO_2$) in the North Atlantic as a function of (a) SST, (b) SSS, (c) DIC, and (d) alkalinity using the mean parameter values of each season for the 2071–2100 period. The circle and triangle markers represent mean values for the r85 and r85ce2 simulations, respectively. (e) The annual mean values for all regions as defined in Figure 5. (f) Map of the difference in $\partial C_T/\partial pCO_2$ between r85ce2 and r85 simulations. Both Figures 8e and 8f show mean values for the 2071–2100 period as well.

under the future RCP8.5 scenario, the NorESM1-ME model projects higher evaporation than precipitation rates in the Atlantic (tropical and midlatitude), leading to more saline surface water with higher alkalinity [*Stott et al.*, 2008; *Tjiputra et al.*, 2014]. Our analysis shows that the SAI-induced lower SST and more efficient transport of DIC from surface to depth explains the stronger carbon uptake in the North Atlantic.

Next, we calculate the annual mean of equation (1) for all seven ocean regions (as defined in Figure 5) from both r85 and r85ce2 simulations for the same 2071–2100 period. As shown in Figure 8e, the consistently colder SST in r85ce2 leads to higher $\partial C_T/\partial pCO_2$ in all regions. Apart from the North and tropical Atlantic, surface DIC is generally higher in the simulation with SAI, hence reducing the $\partial C_T/\partial pCO_2$ term. As seen in the North Atlantic, the regional surface alkalinity signal is the opposite of DIC in other ocean regions and smaller than the DIC signal, except for the North and tropical Atlantic.

Finally, to illustrate the spatial change in the $\partial C_T/\partial pCO_2$ term as a result of climate engineering, we computed equation (1) using long-term (2071–2100) mean values of SST, SSS, DIC, and alkalinity at individual model grid points from each simulation separately. Figure 8f shows a map of the spatial difference (r85ce2 minus r85) of $\partial C_T/\partial pCO_2$ terms. It shows that in high-latitude carbon sink regions, SAI leads to surface ocean state with higher $\partial C_T/\partial pCO_2$ and hence higher uptake efficiency. In contrast, in the low-latitude CO_2 outgassing region, the values are lower in r85ce2 than in r85. This would imply that SAI slows the outgassing rate of carbon in these regions, allowing the ocean to retain more carbon. In both cases, this indicates that during the SAI implementation period, a large part of surface ocean would have the capacity to store slightly more carbon than in the world without SAI.

3.3. Ocean Acidification

One of the consequences of ocean absorption of excess anthropogenic CO_2 from the atmosphere is the perturbed seawater chemistry. As more CO_2 is dissolved in seawater, the carbonate ion concentration decreases and leads to a lower ocean pH. Changes in ocean pH and carbonate ion concentrations beyond their current natural variability could have adverse impact on marine organisms. For example, when the ocean is undersaturated with respect to certain carbonate minerals, key marine organisms such as corals and calcium

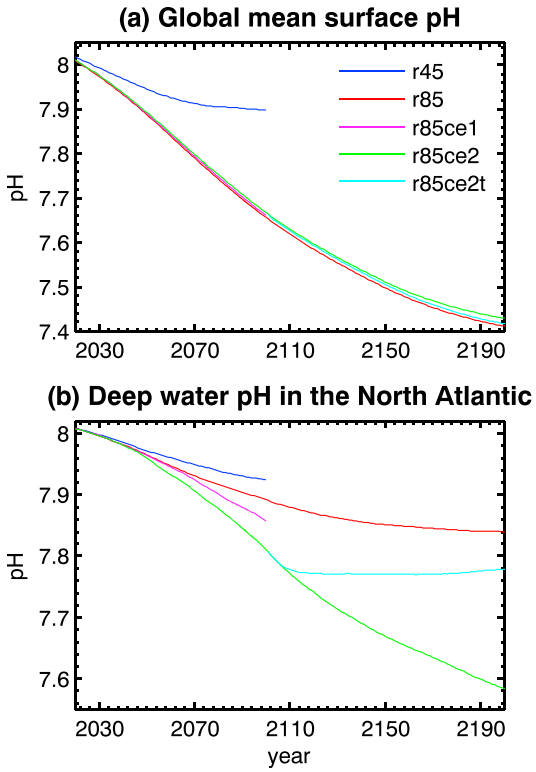

Figure 9. Time series of mean pH for the (a) global surface and (b) deep water in the North Atlantic (>2000 m, 30°N–75°N) between 2020 and 2200 for each simulation.

carbonate-forming plankton will be at risk due to the difficulty in maintaining their external calcium carbonate shells [*Orr et al.*, 2005]. It has also been shown that some calcifying organisms could be more sensitive as they are not found in environments with aragonite saturation state values below 3 [*Kleypas et al.*, 1999; *Meissner et al.*, 2012].

Under the RCP8.5 scenario, CMIP5 models project a robust decline in the global mean surface pH, with the mean expected changes from present days of -0.33 ± 0.003 (1σ) pH unit by the end of the 21st century [*Bopp et al.*, 2013]. Table 2 shows that the NorESM projects a comparable change in r85 simulation (global mean surface pH in year 2000 is 8.06). Figure 9 shows that the surface pH negative trend is slowing down in the 22nd century. And by 2200, the surface pH will be further decreased by 0.25 pH unit under the RCP8.5 scenario (see also Table 2).

Despite the alleviation of temperature increases under the SAI scenario compared to r85, Figure 9a indicates that SAI will not significantly change global surface ocean acidification. This result is consistent with our earlier analysis which shows similar magnitude of oceanic CO_2 sinks globally. Regionally, the model simulates similar evolution of surface pH for the seven ocean domains (not shown). In the 22nd century, there is also negligible change in the projected global mean surface pH regardless whether or not SAI is terminated.

In contrast, the projected pH change in deep water formation region of the North Atlantic is sensitive to SAI. While most of the anthropogenic CO_2 entering the ocean will reside in the near surface water masses, where deep water forms the anthropogenic CO_2 will be transported into depth. Here changes in interior pH amplify with the magnitude of the SAI forcing, as shown in Figure 9b. For the present, the mean deep water (>2000 m) pH in the North Atlantic between 30°N and 75°N is simulated to be 8.01, slightly lower than the preindustrial state of 8.07. By the end of the 21st century, this number is projected to decrease to 7.86 (7.81) in the r85ce1 (r85ce2) simulation, as compared to only 7.89 in the r85 simulation. This sensitivity is related to AMOC strength (see also Figure 2f). Under the baseline r85 simulation, the projected weakening of AMOC reduces the anthropogenic CO_2 transport into depth. Since the AMOC reduction trend is suppressed (r85ce1) and even reversed (r85ce2) in simulations with SAI (for the 21st century), more anthropogenic carbon transported into depth can be expected, leading to a stronger pH reduction.

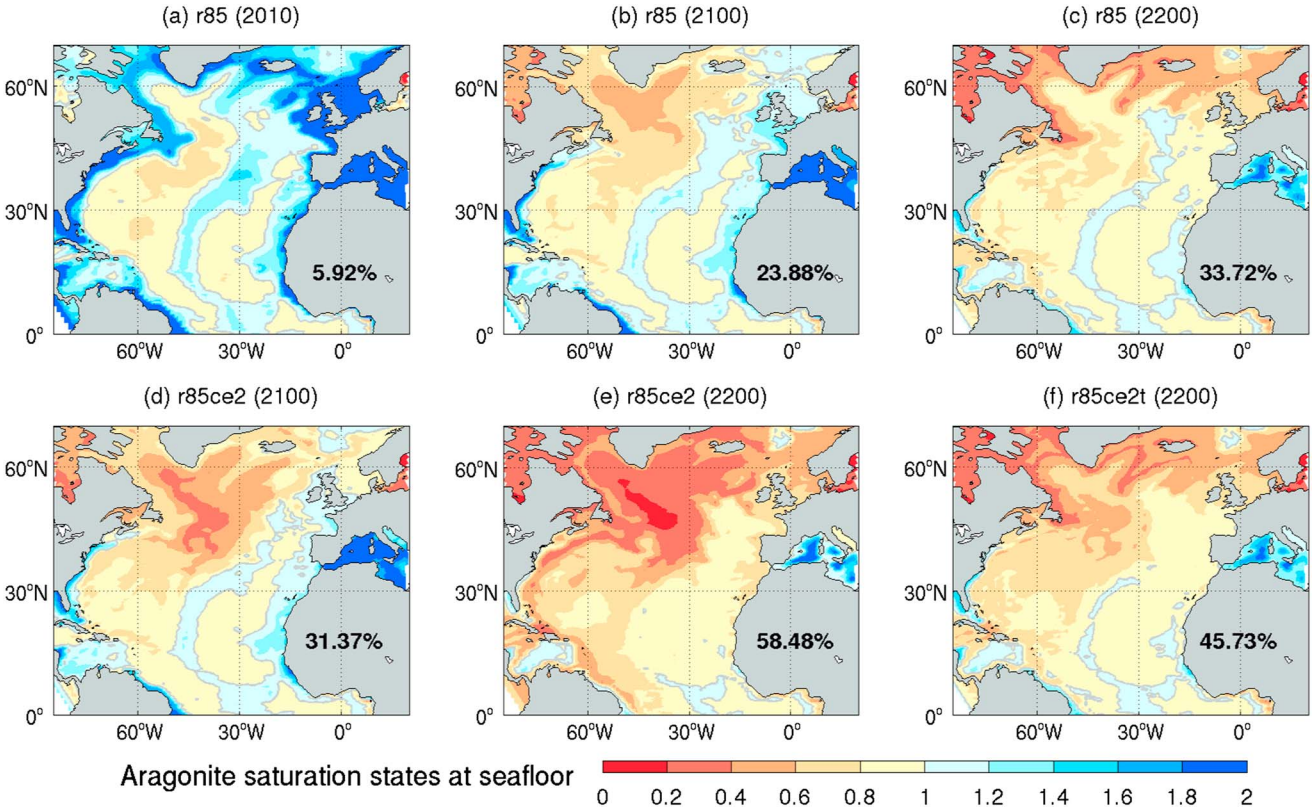

Figure 10. Maps of aragonite saturation states on the North Atlantic seafloor for the baseline RCP8.5 projections in years (a) 2010, (b) 2100, and (c) 2200. The projections under aggressive CE scenario r85ce2 for (d) 2100 and (e) 2200. (f) The projection at 2200 following CE termination in r85ce2t simulation. Grey contour lines represent saturation state at 1.0 values, where values less than 1 represent regions of undersaturation. The numbers inside each panel represents percentage of North Atlantic (north of 0° latitude) seafloor area with saturation state of less than 0.8.

In the 22nd century, r85ce2 continues to simulate a strong pH decline in the deep water of North Atlantic until 2200, reaching a pH value of 7.58. Under the termination branch simulation r85ce2t, pH decline is also projected to continue until around 2110 before it stabilizes at a minimum value of ~7.77 and slowly increases toward the end of the 22nd century. In the baseline r85, the pH decline rate is slowing down and stabilizing at a mean pH of ~7.84 by 2200. Figure 9b shows that even though the pH in r85ce2t slowly recovers following SAI termination, it remains at a severely low level unlikely to be reached on multicentennials time scale in the simulations without SAI.

Habitats in the deep ocean are continuously exposed to stable environmental conditions (e.g., temperature, pressure, and food supply) with relatively less temporal variability than the surface. Therefore, the projected pH reductions could put the biodiversity at risk [*Gehlen et al.*, 2014]. In their study, *Gehlen et al.* [2014] suggest a pH reduction of −0.2 (from the preindustrial state) as a critical threshold which would present risk for marine life on the North Atlantic seafloor. In r85, the mean deep water pH in the North Atlantic (under the preindustrial period, the pH is 8.07) is projected to pass this threshold in year 2118. With SAI, this threshold will be reached 24 (in 2094) and 36 (in 2082) years earlier in simulations r85ce1 and r85ce2, respectively, allowing even shorter time scales for benthic habitats to potentially adapt to the changes.

Seafloor coral habitats are also susceptible to pH changes and hence changes in the aragonite saturation state change. The aragonite saturation states were also computed using the CO2SYS software, by taking into account the simulated changes in temperature, salinity, DIC, and alkalinity, among others. Figure 10 shows the aragonite saturation states of the North Atlantic seafloor in years 2100 and 2200 as projected in our simulations. Figure 10a indicates that by 2100 under the baseline r85, most of the western North Atlantic seabed is projected to be undersaturated with respect to aragonite. By 2200, the affected area extend into the eastern part of the basin with stronger undersaturation north of 60°N latitude, the Baltic Sea, and western Labrador Sea. When SAI is imposed, the affected region increases further south, and stronger undersaturation states occur in the northern part. By 2200, the model suggests that nearly 60% of the North Atlantic seafloor will

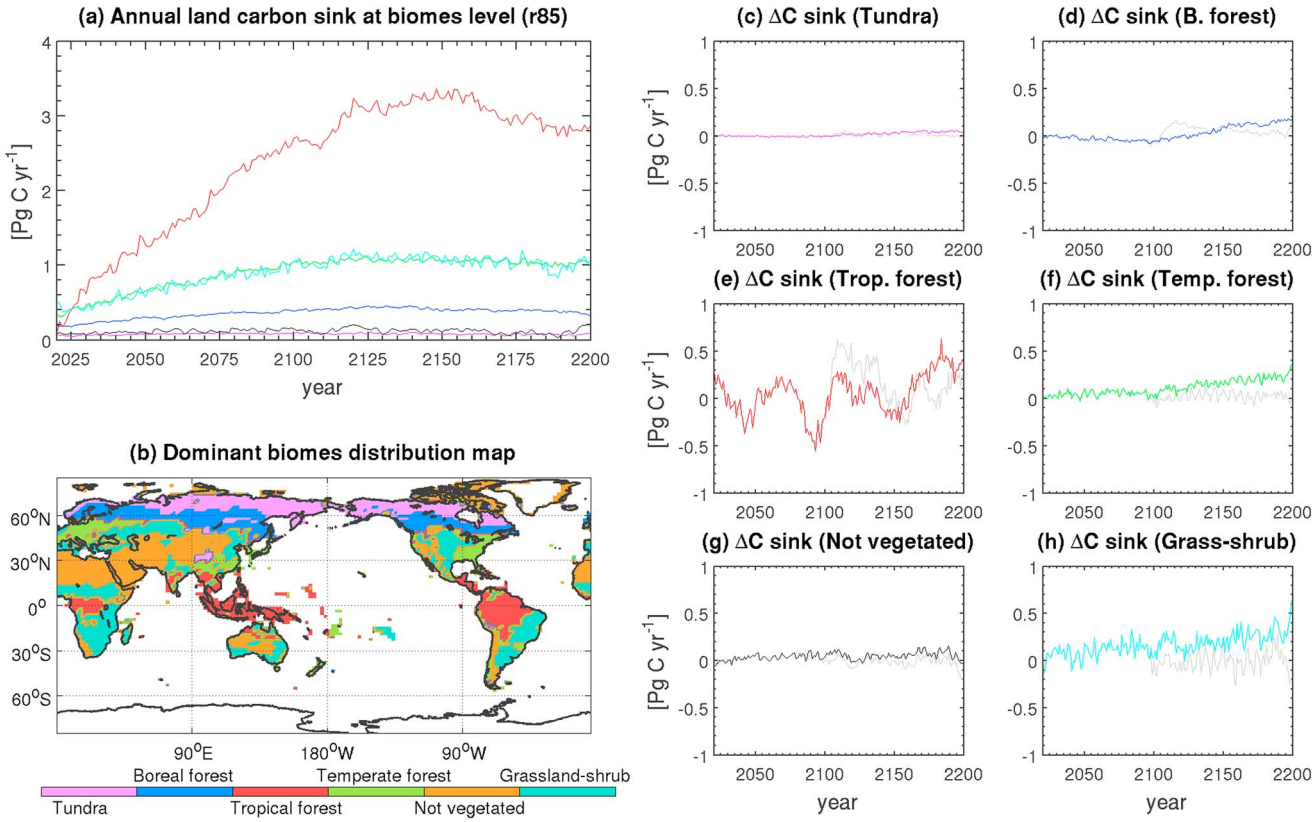

Figure 11. Time series of 9 year running mean annual land carbon uptake at different biomes for the (a) r85 simulation. (b) Map of regions where each biome group dominates. (c–f) The difference between r85ce2 and r85 simulations for each biome, with grey lines indicating the difference between r85ce2t and r85 (2101–2200).

experience aragonite saturation states of less than 0.8 in r85ce2 simulation, whereas without SAI, this number reduces to about 34%. If SAI is discontinued, the projected area with saturation state below this threshold is still about 46% in 2200.

3.4. Changes in Terrestrial Carbon Cycles

Globally, land carbon uptake is also affected by SAI (Table 3). During the SAI implementation (2020–2100), an additional 1% and 2% atmospheric carbon uptake from land was simulated in r85ce1 and r85ce2, respectively. Despite the small difference globally, there are substantial regional differences in the carbon uptake rates (Figure 11). Predominant future uptake occurs in the tropical forest biome, followed by moderate and weaker uptakes in the temperate forest, temperate grassland-shrub, and boreal forest biomes. With SAI, the uptake capacity of tropical forest is substantially perturbed, fluctuating between stronger and weaker sinks at multidecadal time scales. We attribute this large decadal variability to the strong sensitivity of tropical forest to drought and precipitation changes [*Phillips et al.*, 2009] (see also discussion below). The sensitivity of the Amazonian forest in the CLM model to drought has also been evaluated by *Sakaguchi et al.* [2011]. In the 22nd century, the impact of SAI on terrestrial carbon uptake is more pronounced with higher carbon uptake in regions dominated by temperate forest, temperate grassland-shrub, and nonvegetated land areas (i.e., hot and polar deserts).

Under the aggressive SAI scenario (r85ce2), wet tropical climate zones and subarctic climate zones show clear decrease in vegetation carbon storage (Figure 12a), by as much as 2.0 kg C m^{-2} by the end of the 21st century. However, some regions show a slight increase (e.g., southwest North America, South Africa, and southern Europe) and some even increase by as much as 2.0 kg C m^{-2} (northeastern part of the Amazon). This pattern is consistent between r85ce2 and r85ce1 SAI scenarios with approximately a threefold greater magnitude under the aggressive scenario.

There is an overall increase in soil carbon storage (Figure 12d) with SAI, although the magnitude is not as large as that seen in vegetation carbon. Figure 12c also shows that there are few locations where the model projects

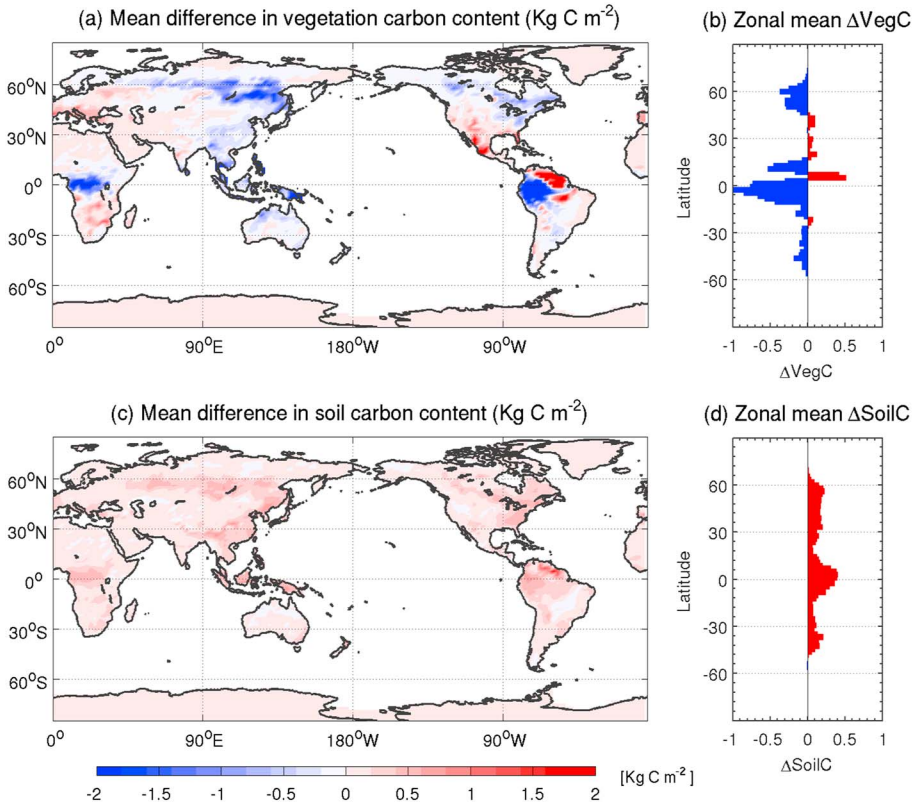

Figure 12. Maps of mean difference in (a) vegetation and (c) soil carbon contents between aggressive CE scenario (r85ce2) and reference RCP8.5 scenario (r85) for the last 30 years of the 21st century (2071–2100). Positive values denote increase in vegetation/soil carbon content in the r85ce2 simulation, whereas negative values otherwise. (b and d) The zonally averaged values for these differences are depicted.

a decrease in soil carbon content. The majority of the areas with a decrease in vegetation carbon storage show an increase in soil carbon storage (e.g., wet tropics and subarctic zone) and most areas that show an increase in vegetation carbon storage also show an increase in soil carbon content (e.g., the eastern Amazon and the Mediterranean regions). The increase is up to 1.0 kg C m^{-2} under the aggressive SAI scenario. This spatial pattern is also similar in both SAI scenarios with greater magnitude of change under the aggressive one.

Interestingly, changes in the patterns of vegetation carbon storage in response to SAI strongly resemble that of precipitation (Figures 12a and 13c). By the end of the 21st century, r85 projects large increases in mean annual precipitation (up to 1000 mm yr^{-1}) in the wet tropical climate zones and the high latitudes. On the other hand, the precipitation in the northeastern Amazon and the Mediterranean regions are projected to decrease. Under the aggressive SAI scenario, these changes are dampened in most regions leading to only small changes. Conversely, the precipitation signal is reversed in regions such as the temperate forest in eastern Asia, North America, and parts of South America (e.g., SAI leads to a reduction rather than increase in mean precipitation; Figures 13a and 13b).

Four domains were selected for the analysis of vegetation carbon, soil carbon, mean annual surface temperature, and mean annual precipitation from the start of the aggressive SAI scenario until 2200 (Figure 14): (1) eastern Siberian boreal forest (hereafter Taiga: 50°N–60°N, 90°E–120°E), (2) northwestern Amazonia (hereafter W Amazon: 10°S–0°N, 285°E–300°E), (3) northeastern Amazonia (hereafter E Amazon: 0°N–10°N, 290°E–305°E), and (4) Spanish Mediterranean (hereafter Mediterranean: 35°N–45°N, 10°W–5°E). The vegetation and soil carbon contents are normalized against the mean state of 2020–2029 (the first 10 years of SAI deployment) to better understand changing trends in terrestrial carbon storage both under increasing atmospheric temperature and the effects of SAI. The above four regions either show a pronounced decrease in vegetation carbon storage but an increase in soil carbon storage (Taiga and W Amazon) or both an increase in vegetation and soil carbon storage (E Amazon and Mediterranean).

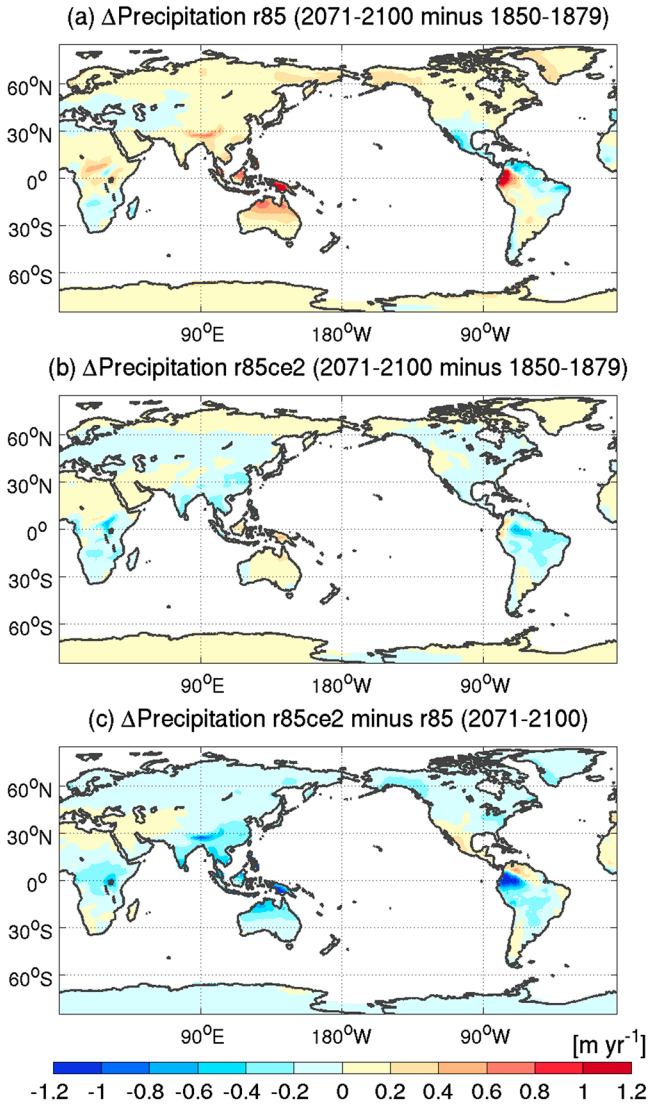

Figure 13. Maps of mean changes in the simulated total precipitation by the end of the 21st century relative to the early preindustrial period for simulations (a) r85 and (b) r85ce2. Positive values denote increase in precipitation. (c) The mean difference between r85ce2 and r85 for the 2071–2100 period.

Vegetation carbon storage under the baseline r85 (Figure 14a, dotted lines) decreases in the E Amazon (blue dotted line; ~2.0 kg C m^{-2}) and increases in Taiga (green dotted line; ~2.0 kg C m^{-2}), whereas W Amazon and Mediterranean remain stable until 2100. Under the aggressive SAI scenario (r85ce2), vegetation carbon storage increases in E Amazon but decreases drastically in W Amazon (red solid line; ~4.0 kg C m^{-2}), whereas Taiga and Mediterranean do not show much change until 2100. This is due to combined effects of temperature and precipitation patterns under r85 and r85ce2 (Figures 14a, 14c, and 14d). For instance, regions where vegetation growth is limited by temperature (Taiga) are more sensitive to increases in surface temperature, whereas the response of vegetation carbon storage in tropical regions such as the Amazonia are more sensitive to precipitation. Other tropical regions (i.e., central Africa and Southeast Asia) with a reduced vegetation carbon pool also demonstrate similar relationships with precipitation changes (not shown). This highlights the importance of SAI-induced changes in precipitation when considering future carbon changes in vegetation.

Soil carbon storage is more sensitive to changes in surface temperature than precipitation (Figure 14b) compared to vegetation carbon storage. There is an overall decrease in soil carbon storage in all four regions investigated (e.g., a ~2.0 kg C m^{-2} decrease in E Amazon by the year 2200) with the projected increase in surface temperature from the baseline r85 simulation. With SAI, soil carbon storage slightly increases probably

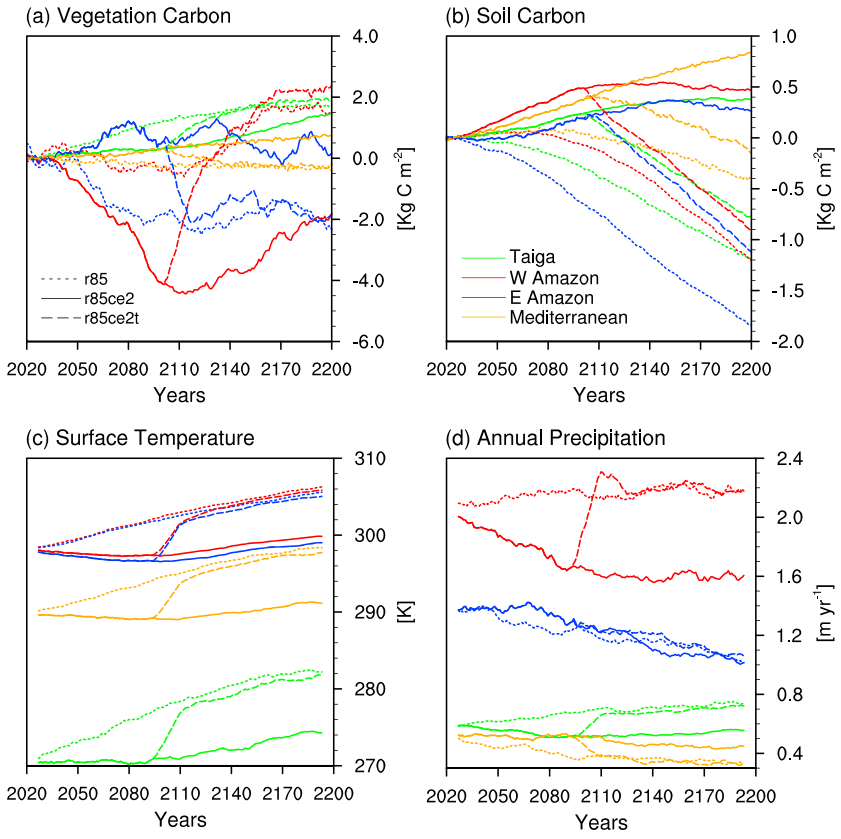

Figure 14. Time series of (a) vegetation carbon, (b) soil carbon, (c) surface temperature, and (d) annual precipitation for the reference RCP8.5 scenario (r85, dotted lines) and the aggressive CE scenario (r85ce2, solid lines). The dashed lines represent projections following CE termination (r85ce2t). The four regions shown here are Taiga (green: 50°N–60°N, 90°E–120°E), W Amazon (red: 10°S–0°N, 285°E–300°E), E Amazon (blue: 0°N–10°N, 290°E–305°E), and Mediterranean (yellow: 35°N–45°N, 10°W–5°E). Values in Figures 14a and 14b are normalized against the mean of first 10 years of the simulation (2020–2029). Figures 14c and 14d represent 15 year running average.

due to stabilized surface temperature. Previous studies also suggest that cooler temperature leads to a reduction in heterotrophic respiration, allowing the soil to retain more carbon [e.g., *Jones and Cox*, 2001; *Brovkin et al.*, 2010].

Upon SAI termination (r85ce2t, dashed lines in Figure 14), vegetation carbon storage shows a drastic shift when surface temperature and precipitation levels quickly catch up with the baseline r85. Interestingly, vegetation carbon in Taiga in simulations with SAI becomes greater than that without by the end of 22nd century. This is also the case even when surface temperature is still approximately 0.5 K lower under the SAI scenario. The E Amazon responds differently to the other tropical regions. Here there is a rapid decline in vegetation carbon following SAI termination despite no significant changes in precipitation. In the next 100 years following SAI termination, the cumulative land carbon sink is higher by 4% and there is a steep decline in soil carbon storage. Unlike vegetation carbon storage, soil carbon storage benefits from SAI and shows higher soil carbon storage in all regions by the end of 22nd century. When SAI is continued until 2200 (r85ce2, solid lines in Figure 14), vegetation carbon maintains similar trends to the previous century except in W Amazon where vegetation carbon starts to increase. The soil carbon storage starts to plateau in the early 22nd century except the Mediterranean, where it continues to increase.

On a global scale, total vegetation (soil) carbon decreases (increases) by 26 (28) Pg C under the aggressive SAI scenario compared to non-SAI scenario by 2100. When SAI is continued until 2200, vegetation carbon storage is similar to the non-SAI scenario but global soil carbon is greater by 60 Pg C. Even if SAI is terminated, the total global vegetation carbon storage is still greater by 10 Pg C and soil carbon storage is greater by 14 Pg C in 2200.

4. Discussion

Understanding how the global carbon cycle would respond to climate engineering is important for policy makers when planning for future climate mitigation and adaptation strategies. We apply a state-of-the-art Earth system model to simulate artificial solar radiation management-based climate engineering on top of the RCP8.5 future scenario. We prescribed increasing stratospheric sulfur aerosol concentration to reduce insolation, hence counteracting the climate warming associated with increasing atmospheric CO_2 concentration. This method, often referred to as stratospheric aerosol injection (SAI), is considered as one of the few schemes to potentially produce effective large-scale cooling of the planet. However, currently, there is no technology to conduct SAI [*Robock*, 2014].

We investigated two SAI scenarios with a different magnitudes of the prescribed aerosol concentrations: medium and aggressive. Each SAI scenario was applied on top of the future RCP8.5 scenario simulation. In the medium case, the projected global warming rate slows down to the rate projected under the RCP4.5 scenario. Nevertheless, our method is shown to be less efficient in suppressing the warming at polar regions, consistent with an earlier study of *Berdahl et al.* [2014]. In the aggressive scenario, the model projects a negative temperature trend, reversing the earlier global temperature increase, toward 2100.

During SAI implementation (2020–2100), the ocean becomes a stronger sink for carbon. In the tropical Atlantic, tropical Pacific, and North Atlantic domains, the cumulative ocean carbon sinks increase by 45%, 40%, and 12%, respectively. In the tropical oceans, this is partly attributed to the higher biological export production. In the simulation without SAI, biological productivity in the tropical ocean decreases due to stronger stratification and less nutrient supply from depth. In addition, SAI-induced cooler SSTs in the tropical upwelling region allows for a higher solubility of CO_2 gas in seawater, which leads to a weaker CO_2 outgassing. In the North Atlantic, SAI preserves high overturning strength, allowing for more efficient transport of dissolved inorganic carbon into the ocean interior through deep water formation.

The artificial SAI also alleviates the sea ice reduction projected in RCP8.5, delaying the ice-free summer condition by some years. Changes in the sea ice extent, in turn, alters the air-sea CO_2 fluxes and net primary production. In the model, sea ice acts as an impermeable lid for air-sea gas exchange; therefore, carbon sinks around the sea ice edges are expected to decline with SAI. Cooler SSTs associated with the delay in melting of sea ice also limits the phytoplankton growth rate in high latitudes.

Our simulations show that SAI will not alter the surface ocean acidification. However, in the interior North Atlantic the model projects significant and long-lasting excursions in the deep water pH when SAI is implemented. This effect is related to the stronger deep water formation, allowing more anthropogenic CO_2 to enter the deep ocean. In the aggressive SAI scenario, the model predicts that the deep water environment will reach a critical pH threshold, potentially damaging susceptible benthic habitats 34 years earlier than in the reference simulation. The negative effect of seabed ocean acidification is predicted to be stronger and more widespread when we consider SAI in the future. Since the deep ocean provides vital ecosystem function and services, e.g., fish stocks, this accelerated changes could introduce broader impacts on human welfare [*Thurber et al.*, 2014].

In the 21st century, the projected global terrestrial carbon sink shows little response to SAI, even in the aggressive scenario. This could be attributed to the strong nitrogen limitation, which is a characteristic of the CLM4 land model [*Lindsay et al.*, 2014]. We note that due to the lower atmospheric CO_2 concentration in simulations with SAI, it is expected that the CO_2 fertilization effect on the terrestrial biosphere is weaker, hence lowering the net primary production. Nevertheless, earlier studies show that the nitrogen limitation in the NorESM1-ME model dominates over the CO_2 fertilization effect [*Arora et al.*, 2013; *Bonan and Levis*, 2010]. We show that the regional changes in the land net primary production can be predominantly attributed to the regional temperature and precipitation signals.

The projected changes in spatial vegetation and soil carbon storage due to SAI depend on the simulated soil temperature and precipitation trends. Our results show that SAI-induced cooling leads to less heterotrophic respiration in the soil, allowing higher carbon retention in nearly all regions with high soil density. We show that the projected changes in vegetation carbon is particularly sensitive to the precipitation change in most regions: regions with increased precipitation as a consequence of SAI are generally projected to show increased vegetation carbon storage, and vice versa.

If SAI is continued into the 22nd century, the model projects that the ocean will continue to increase the carbon uptake rate, and by 2200 the pH in the deep water of the North Atlantic would decline by 0.43 pH unit compared to only 0.17 pH unit if SAI is not deployed. As the temperature slowly rises in response to the higher atmospheric CO_2 burden, the soil carbon content stabilizes and the vegetation carbon steadily increases, especially in the tropics. This leads to a net increase in land carbon sink.

Currently, there is no proven technology in existence that allows for a large-scale SAI implementation. There are also many unknown and unexpected side effects of SAI. Thus, a termination of SAI at some point must be considered as a plausible option. Our model simulations show that following termination of SAI, the temperature and precipitation signals rapidly regress to the non-SAI climate. Both the ocean and terrestrial carbon uptake rates also return to that simulated in the non-SAI scenario. The same responses are also projected in the vegetation and soil carbon pools, although the latter occur at a slower rate. This implies that future large-scale cooling related to SAI would be short lived and likely to have a reversible impact on the land and ocean carbon uptakes. Thus, SAI-induced cooling would not substantially alter future climate-carbon cycle feedbacks, which will be dominated by the strong background warming trend associated with the high anthropogenic CO_2 emission rate. Therefore, concrete strategies to significantly lower or reverse the ongoing anthropogenic CO_2 emissions is undoubtedly necessary, regardless of SAI deployment (or application). Additionally, prior to any SAI deployment, a strategically designed and rigorously tested global monitoring system will need to be in place to ensure close observation and early warning of changes in the climate system.

4.1. Comparison With Previous Studies

We note that the idealized SAI experiments in this study are not directly comparable with other SAI or SRM scenarios documented in earlier work, generally because of the differences in model complexity and experimental design (see also section 1). Despite these differences, similarities, and inconsistencies between the studies with respect to SAI-induced changes in key climate metrics and respective impacts on the global carbon cycle are presented in this subsection.

Compared to other SRM modeling studies, such as *Kravitz et al.* [2013], the projected cooler surface air temperature in our study is generally consistent with stronger cooling at high latitudes. Relative to the preindustrial state, we also show that SAI is less efficient in suppressing the warming in the polar regions [*Kravitz et al.*, 2013; *Berdahl et al.*, 2014]. The regional precipitation response is more diverse among the different models, but globally, SAI is projected to decrease the precipitation [*Jones et al.*, 2013]. Figure 13b shows that our model indeed simulates reduction in precipitation over large parts of the land.

In previous studies with a fully interactive model configuration (i.e., prognostic atmospheric CO_2), SRM-type CE leads to a lower atmospheric CO_2 concentration due to enhanced carbon sinks either into land, ocean, or both. For instance, using EMIC-type models, *Matthews and Caldeira* [2007] and *Keller et al.* [2014] apply artificial SRM to the future high-CO_2 scenario and project lower atmospheric CO_2 concentrations by 2100. *Keller et al.* [2014] attribute this predominantly to the enhanced carbon sink by the terrestrial biosphere, whereas *Matthews and Caldeira* [2007] only indicate that both the land and ocean have higher carbon sinks in response to increasing atmospheric CO_2 concentration. As both use the same model (i.e., UVic-ESCM), it is perhaps not surprising that similar patterns were simulated. Since their land models do not include nitrogen limitation, it can be expected that the land carbon sink would response more strongly than the ocean. This is because the CO_2 fertilization effect could overestimate the terrestrial NPP, and hence the carbon sink responses (see next paragraph). In our study, SAI is also shown to reduce the atmospheric CO_2 concentration. However, this is largely attributed to the stronger ocean carbon sink, consistent with the fact that our land model includes nitrogen coupling for the NPP computation.

In our study, SAI impacts the terrestrial carbon cycle generally through increasing NPP in midlatitudes and in parts of the tropics. Comparing the responses of terrestrial NPP from a set of idealized SRM simulations within the GeoMIP project, *Kravitz et al.* [2013] also show an increase in regional NPP primarily due to CO_2 fertilization, and partly to a reduced plant heat stress. Also based on the GeoMIP simulations, *Jones et al.* [2013] show that models with nitrogen limitation are less sensitive to SRM forcing than those without. In a study where a doubled-CO_2 climate is stabilized by idealized geoengineering, *Govindasamy et al.* [2002] also confirm that without nutrient limitation, the CO_2 fertilization effect dominates the terrestrial biosphere response, leading to nearly doubled NPP and biomass. Therefore, improved understanding on how SRM may alter the terrestrial nitrogen cycle is critical to determine the overall carbon cycle response. Note that it has also been shown

that increase in diffusive light (i.e., due to increase stratospheric aerosol concentration) may also increase NPP [*Mercado et al.*, 2009]. Our simulations include regional changes in diffusive light, but the current study is unable to isolate this effect on the NPP.

Regionally, we show that SAI decreases the land carbon sinks in the tropical and boreal forests and increases in the grasslands, deserts, and temperate forest. This finding is consistent with *Naik et al.* [2003], despite the fact that they use a different model. We show that regional vegetation carbon changes due to SAI broadly resemble changes in precipitation. This result supports a recent SRM modeling study based on marine sky brightening by *Muri et al.* [2015], which emphasizes the importance of SRM-induced precipitation changes on terrestrial productivity, especially in the tropics. In the northern high latitudes, *Govindasamy et al.* [2002] show that SRM leads to a slightly lower increase in vegetation biomass due to a cooler and drier climate. This pattern is similar with our simulation (see Figure 14a, green lines). In addition to changes in land NPP, we show that the SAI-induced cooler climate reduces the land release of CO_2 because of a lower heterotrophic soil respiration rate in most regions, also in agreement with the findings by *Keller et al.* [2014].

There are fewer modeling studies that have analyzed the ocean carbon cycle response to SRM than its land counterpart. In simulations where the atmospheric CO_2 is prescribed, it is expected that cooling due to SRM would cool the SST, leading to a higher CO_2 solubility and hence a stronger ocean carbon sink, though changes in ocean circulation and biological production could also play an important role. With prognostic atmospheric CO_2, the changes in ocean carbon sink also depend on how the atmospheric CO_2 level response to SRM [*Matthews et al.*, 2009]. This is because the ocean carbon uptake rate also depends on the atmospheric-ocean gradient of CO_2 partial pressure. The atmospheric CO_2, in turn, also depends on how sensitive the land carbon uptake is to SRM. Models where the land carbon uptakes increase strongly to SRM forcing (e.g., due to lack of nitrogen limitation, see also above) are expected to project little change in the ocean carbon sink because the difference between ocean-atmosphere partial pressure of CO_2 becomes weaker [*Matthews et al.*, 2009; *Keller et al.*, 2014]. Our simulated land carbon sink is less sensitive to SAI, and consequently, a stronger increase in ocean carbon sink occurs.

We also acknowledge the potential for a large amount of carbon release in the high-latitude permafrost region in response to future climate warming and that this feedback to climate could be altered considerably with SAI. However, we are unable to quantify this as our land model does not have the ability simulate and quantify permafrost-related climate feedbacks.

Our results for the SAI impact on surface ocean acidification are consistent with *Matthews et al.* [2009] and *Keller et al.* [2014], in that SRM-type CE will not substantially alter the projected surface pH since the anthropogenic CO_2 emissions are the primary driver for ocean acidification. In their SRM simulations, the projected surface pH is only slightly higher relative to the non-SRM reference case. The lower surface pCO_2 due to the lower atmospheric CO_2 is compensated by the higher surface dissolved inorganic carbon concentration in response to higher CO_2 solubility (due to cooler SSTs). For the deep ocean, our study is the first to highlight that SRM-type CE will introduce stronger ocean acidification in the interior ocean, especially near deep water formation regions. Presently, the water mass in the North Atlantic interior is simulated to have decreased by 0.03 pH unit from the preindustrial state. By 2100 under RCP8.5 scenario, it is projected to further decrease by 0.12 pH unit, or by 0.20 pH units if aggressive SAI is deployed.

Following SAI termination, our analysis is in agreement with *Jones et al.* [2013] study with GeoMIP models in that the land carbon cycle responses vary between models depending on the changes in precipitation patterns. In connection to the rapid warming that occurs following SAI termination, we simulate a steady loss of soil carbon due to accelerating soil decomposition, as also shown by *Jones et al.* [2013]. In the study by *Keller et al.* [2014], once SAI is discontinued, the atmospheric CO_2 steadily rebounded to the nongeoengineered state. Here the atmospheric CO_2 also rebounds but continues to stay lower than the non-SAI case. The ocean carbon sink is weaker after SAI termination, but the land carbon sink is higher (relative to the non-SAI case). The latter is attributed to the higher NPP in the tropical forest biome due to the strong response of the simulated precipitation to SAI termination (see also Figure 14d).

4.2. Limitations and Uncertainties

We note that our results only represent simulations from one model. Ideally, a set of similar SAI experiments with different model systems is required to confirm the robustness of the projected signals as well as to better understand the sensitivity of different land and ocean biogeochemical parameterization to the

regional climate change (e.g., ocean circulation, surface temperature, and precipitation). In the case of terrestrial vegetation response, a multimodel ensemble approach employing land models with a nitrogen cycle is needed.

Our SAI experiments are based on an idealized configuration and ignore the evolution of aerosol particle size in the stratosphere. In reality, higher aerosol concentrations leads to particle coagulation and larger particle sizes, which reduce the aerosol efficiency in scattering incoming short-wave radiation [*Niemeier et al.*, 2011]. Here we acknowledge that our simplistic Pinatubo-based forcing considers the observed seasonal and spatial (i.e., interhemispheric asymmetry) variations in the aerosol concentration, which is likely to be very different from the more representative forcing [e.g., *Ferraro et al.*, 2014; *Tilmes et al.*, 2015]. These spatial and temporal differences could substantially influence the climate responses over the tropical and subtropical land and ocean regions. For example, in an extreme case, *Haywood et al.* [2013] show that sulfate aerosol geoengineering in the Northern Hemisphere versus Southern Hemisphere would introduce very large difference in precipitation response in the Sahel region.

Our method also does not take into account potential climate feedbacks due to aerosol interaction with ozone. Using a 3-D general circulation model, *Rozanov et al.* [2002] show that interactive stratospheric chemistry together with the Pinatubo eruption would deplete ozone due to heterogeneous chemistry on the volcanic aerosols and changed photolysis rates. Stratospheric ozone depletion would lead to lower heating rates in the stratosphere. However, *Rozanov et al.* [2002] found that the change of radiative heating rates due to the ozone change was less important than the heating due to the aerosols themselves. In a similar study, but using a 2-D model, *Rosenfield et al.* [1997] found that most of the stratospheric ozone change at low latitudes was due to circulation changes caused by radiative heating from the stratospheric aerosol. We note that when different aerosol forcing (than that applied in this study) is used, a different response particularly on the terrestrial carbon cycle might be expected.

The weak land carbon response to SAI is likely to be attributed to the inclusion of nitrogen limitation in the NorESM1-ME model. A recent study by *Thomas et al.* [2013] indicates that the nitrogen limitation in CLM-CN4.0 (i.e., the land component of the NorESM1-ME) is generally more sensitive as compared to the field observations, specifically in the temperate and boreal forest regions. The CLM-CN model simulates higher increase in aboveground NPP (than observed) in response to nitrogen fertilization. They also hinted at potential reasons for the simulated high sensitivity, which if calibrated would better constrain the productivity response to nitrogen perturbation.

The CLM-CN prescribes annual transient land cover change that comprises changes in plant functional type (PFT) and wood harvest for the historical and RCP scenarios. The carbon emissions associated with this land cover change were computed by taking into account the prognostic climate states as documented in *Lawrence et al.* [2012]. In all of our future scenario simulations with SAI, we apply the same RCP8.5 transient land cover change in which the associated carbon emissions are not significantly perturbed (not shown). In the real world, SAI-induced large climatic change also affects the land cover through changes in PFT and wood harvest distribution, which could have additional implications on the land carbon cycle. In addition to land cover change, we consider nitrogen limitation and vegetation responses to precipitation changes to be the major source of uncertainty when determining the land carbon cycle response to SAI. As noted above, the precipitation along with other climatic responses in some regions will also depend on the SAI forcing applied. Therefore, studies that evaluate the sensitivity of terrestrial biogeochemistry response to SAI scenarios with different spatial and temporal aerosol patterns will be useful to assess the robustness of our simulated signals.

With respect to the stronger acidification in the deep water of North Atlantic due to SAI, we note that the NorESM1-ME model has an anomalously strong AMOC strength [*Bentsen et al.*, 2013]. Thus, the affected seafloor area may be smaller for other models with weaker AMOC. The NorESM1-ME model also lacks dynamic ice sheets over land that would allow for a large-scale melting in response to climate change. This effect could alter the ocean ventilation at high latitudes and in turn the air-sea carbon fluxes, among others.

Our study focuses on evaluating the SAI-based climate engineering (CE) impact on future global biogeochemical cycles. Impacts on other aspects of the climate system, directly affecting society such as extreme weather events, the hydrological cycles, agriculture, and fisheries, are far from well understood. Other issues such as governance, ethical, and societal perception of CE also need to be carefully assessed. There are also other CE techniques, for instance, ocean fertilization, enhanced mineral weathering, and marine cloud brightening

[e.g., *Ilyina et al.*, 2013; *Scott et al.*, 2013; *Keller et al.*, 2014; *Muri et al.*, 2015]. These techniques will have different impacts on the Earth system, and if deployed together, their accumulated impact is unlikely to be linear. This calls for further scientifically based assessments for each individual CE technique, and in combination.

5. Concluding Remarks

Future climate engineering based on an idealized stratospheric aerosol injection concept is simulated using a state-of-the-art Earth system model. The artificial SAI forcing is included in the future projection under the high CO_2 emissions scenario RCP8.5, leading to a suppressed future warming. We found that SAI could have a profound impact on both the future terrestrial and ocean carbon cycle. On land, changes in temperature and precipitation patterns alter carbon sequestration through changing the soil respiration and net primary production rates. Changes in sea surface temperature, sea ice extent, and ocean circulation predominantly drive regional changes in ocean carbon sinks and sequestrations and, consequently, alter ocean acidification in the interior ocean.

The global carbon cycle response to SAI will depend on the sensitivity of the terrestrial processes. When nutrient limitation over land is considered, there is a weak response on the land carbon sinks to SAI. This effect, combined with SAI-induced cooler SSTs, leads to increase in CO_2 gas solubility in seawater, hence increasing anthropogenic carbon invasion into the ocean. Nevertheless, this additional net increase is insufficient to lower the atmospheric CO_2 considerably. Therefore, once the SAI is discontinued, global temperatures rapidly rebound toward the nongeoengineered climate.

Acknowledgments
This research was supported by the Norwegian Research Council through the EXPECT and ORGANIC projects (grants 229760/E10 and 239965/RU). We are grateful and thankful to two anonymous reviewers for their thorough reviews and suggestions, which improve the manuscript substantially. We would like to thank Catherine Bradshaw, Paul Hezel, and Siv Lauvset for reviewing the manuscript.
We acknowledge support by the Norwegian Research Council's program for supercomputing (NOTUR) projects NN2345K, NN9182K, and NN1002K, as well as data storage (NorStore) projects NS2345K, NS9033K, and NS1002K. This is a contribution from the BIOFEEDBACK project of the Centre for Climate Dynamics at Bjerknes Centre. The model data used in this study are long-term archived at the Norwegian Storage Infrastructure project (NorStore) for at least 5 years following publication and will be made available upon request.

References

Ammann, C. M., G. A. Meehl, W. M. Washington, and C. S. Zender (2003), A monthly and latitudinally varying volcanic forcing dataset in simulations of 20th century climate, *Geophys. Res. Lett.*, *30*(12), 1657, doi:10.1029/2003GL016875.
Arora, V. K., et al. (2013), Carbon-concentration and carbon-climate feedbacks in CMIP5 Earth system models, *J. Clim.*, *26*, 5289–5314.
Assmann, K. M., M. Bentsen, J. Segschneider, and C. Heinze (2010), An isopycnic ocean carbon cycle model, *Geosci. Model Dev.*, *3*, 143–167.
Bentsen, M., et al. (2013), The Norwegian Earth System Model, NorESM1-M—Part 1: Description and basic evaluation of the physical climate, *Geosci. Model Dev.*, *6*, 687–720, doi:10.5194/gmd-6-687-2013.
Berdahl, M., A. Robock, D. Ji, J. C. Moore, A. Jones, B. Kravitz, and S. Watanabe (2014), Arctic cryosphere response in the Geoengineering Model Intercomparison Project G3 and G4 scenarios, *J. Geophys. Res. Atmos.*, *119*, 1308–1321, doi:10.1002/2013JD020627.
Bonan, G. B., and S. Levis (2010), Quantifying carbon-nitrogen feedbacks in the Community Land Model (CLM4), *Geophys. Res. Lett.*, *37*, L07401, doi:10.1029/2010GL042430.
Bopp, L., et al. (2013), Multiple stressors of ocean ecosystems in the 21st century: Projections with CMIP5 models, *Biogeosciences*, *10*, 6225–6245, doi:10.5194/bg-10-6225-2013.
Brovkin, V., S. J. Lorenz, J. Jungclaus, T. Raddatz, C. Timmreck, C. H. Reick, and J. Segschneider (2010), Sensitivity of a coupled climate-carbon cycle model to large volcanic eruptions during the last millennium, *Tellus B*, *62*, 674–681, doi:10.1111/j.1600-0889.2010.00471.x.
Collins, M., et al. (2013), Long-term climate change: Projections, commitments and irreversibility, in *Climate Change 2013: The Physical Science Basis. Contribution of Working Group I to the Fifth Assessment Report of the Intergovernmental Panel on Climate Change*, edited by T. F. Stocker et al., Cambridge Univ. Press., Cambridge, U. K., and New York.
Conway, T. J., P. P. Tans, L. S. Waterman, K. W. Thoning, D. R. Kitzis, K. A. Masarie, and N. Zhang (1994), Evidence of interannual variability of the carbon cycle from the NOAA/CMDL global air sampling network, *J. Geophys. Res.*, *99*, 22,831–22,855.
Crutzen, P. J. (2006), Albedo enhancement by stratospheric sulfur injections: A contribution to resolve a policy dilemma?, *Clim. Change*, *77*, 211–219.
DeVries, T., F. Primeau, and C. Deutsch (2012), The sequestration efficiency of the biological pump, *Geophys. Res. Lett.*, *39*, L13601, doi:10.1029/2012GL051963.
Dickson, A. G., and F. J. Millero (1987), A comparison of the equilibrium constants for the dissociation of carbonic acid in seawater media, *Deep Sea Res., Part A*, *34*, 1733–1743.
Etheridge, D. M., L. P. Steele, R. L. Langenfelds, R. J. Francey, J.-M. Barnola, and V. I. Morgan (1996), Natural and anthropogenic changes in atmospheric CO_2 over the last 1000 years from air in Antarctic ice and firn, *J. Geophys. Res.*, *101*(D2), 4115–4128.
Ferraro, A. J., E. J. Highwood, and A. J. Charlton-Perez (2014), Weakened tropical circulation and reduced precipitation in response to geoengineering, *Environ. Res. Lett.*, *9*, 014001, doi:10.1088/1748-9326/9/1/014001.
Frölicher, T. L., M. Winton, and J. L. Sarmiento (2013), Continued global warming after CO_2 emissions stoppage, *Nat. Clim. Change*, *4*, 40–44, doi:10.1038/NCLIMATE2060.
Gehlen, M., et al. (2014), Projected pH reductions by 2100 might put deep North Atlantic biodiversity at risk, *Biogeosciences*, *11*, 6955–6967.
Gent, P. R., et al. (2011), The Community Climate System Model version 4, *J. Clim.*, *24*, 4973–4991, doi:10.1175/2011JCLI4083.1.
Gillett, N. P., V. K. Arora, K. Zickfeld, S. J. Marshall, and W. J. Merryfield (2011), Ongoing climate change following a complete cessation of carbon dioxide emissions, *Nat. Geosci.*, *4*, 83–87, doi:10.1038/ngeo1047.
Govindasamy, B., S. Thompson, P. B. Duffy, K. Caldeira, and C. Delire (2002), Impact of geoengineering schemes on the terrestrial biosphere, *Geophys. Res. Lett.*, *29*(22), 2061, doi:10.1029/2002GL015911.
Haywood, J. M., A. Jones, N. Bellouin, and D. Stephenson (2013), Asymmetric forcing from stratospheric aerosols impacts Sahelian rainfall, *Nat. Clim. Change*, *3*, 660–665, doi:10.1038/nclimate1857.
Heinze, C., S. Meyer, N. Goris, L. Anderson, R. Steinfeldt, N. Chang, C. Le Quéré, and D. C. E. Bakker (2015), The ocean carbon sink—Impacts, vulnerabilities and challenge, *Earth Syst. Dyn.*, *6*, 327–358, doi:10.5194/esd-6-327-2015.
Hoffman, F. M., et al. (2014), Causes and implications of persistent atmospheric carbon dioxide biases in Earth system models, *J. Geophys. Res. Biogeosci.*, *119*, 141–162, doi:10.1002/2013JG002381.

Ilyina, T., D. Wolf-Gladrow, G. Munhoven, and C. Heinze (2013), Assessing the potential of calcium-based artificial ocean alkalinization to mitigate rising atmospheric CO_2 and ocean acidification, *Geophys. Res. Lett.*, *40*, 5909–5914, doi:10.1002/2013GL057981.

Intergovernmental Panel on Climate Change (IPCC) (2012), Meeting report of the Intergovernmental Panel on Climate Change expert meeting on geoengineering, in *IPCC Expert Meeting on Geoengineering, Lima, Peru, 20–22 Jun.*, edited by O. Edenhofer, 99 pp., IPCC Working Group III Tech. Support Unit, Potsdam Inst. for Clim. Impact Res., Potsdam, Germany.

Intergovernmental Panel on Climate Change (IPCC) (2013), Summary for policymakers, in *Climate Change 2013: The Physical Science Basis. Contribution of Working Group I to the Fifth Assessment Report of the Intergovernmental Panel on Climate Change*, edited by T. F. Stocker et al., pp. 1–30, Cambridge Univ. Press., Cambridge, U. K., and New York.

Jones, C. D., and P. M. Cox (2001), Modeling the volcanic signal in the atmospheric CO_2 record, *Global Biogeochem. Cycles*, *15*, 453–465, doi:10.1029/2000GB001281.

Jones, A., et al. (2013), The impact of abrupt suspension of solar radiation management (termination effect) in experiment G2 of the Geoengineering Model Intercomparison Project (GeoMIP), *J. Geophys. Res. Atmos.*, *118*, 9743–9752, doi:10.1002/jgrd.50762.

Jones, C., et al. (2013), Twenty-first-century compatible CO_2 emissions and airborne fraction simulated by CMIP5 Earth system models under four representative concentration pathways, *J. Clim.*, *26*, 4398–4413, doi:10.1175/JCLI-D-12-00554.1.

Keith, D. W., R. Duren, and D. G. MacMartin (2014), Field experiments on solar geoengineering: Report of a workshop exploring a representative research portfolio, *Philos. Trans. R. Soc. A*, *372*, 20140175, doi:10.1098/rsta.2014.0175.

Keller, D. P., E. Y. Feng, and A. Oschlies (2014), Potential climate engineering effectiveness and side effects during a high carbon dioxide-emission scenario, *Nat. Commun.*, *5*, 3304, doi:10.1038/ncomms4304.

Kennedy, J. J., N. A. Rayner, R. O. Smith, M. Saunby, and D. E. Parker (2011), Reassessing biases and other uncertainties in sea surface temperature observations measured in situ since 1850 part 2: Biases and homogenisation, *J. Geophys. Res.*, *116*, D14104, doi:10.1029/2010JD015220.

Kirkevåg, A., et al. (2013), Aerosol-climate interactions in the Norwegian Earth System Model—NorESM1-M, *Geosci. Model Dev.*, *6*, 207–244, doi:10.5194/gmd-6-207-2013.

Kleypas, J. A., J. W. McManus, and L. A. B. Menez (1999), Environmental limits to coral reef development: Where do we draw the line?, *Am. Zool.*, *39*, 146–159.

Kravitz, B., A. Robock, P. M. Forster, J. M. Haywood, M. G. Lawrence, and H. Schmidt (2013), An overview of the Geoengineering Model Intercomparison Project (GeoMIP), *J. Geophys. Res. Atmos.*, *118*, 13,103–13,107, doi:10.1002/2013JD020569.

Lawrence, D., et al. (2011), Parameterization improvements and functional and structural advances in version 4 of the Community Land Model, *J. Adv. Model. Earth Syst.*, *3*, M03001, doi:10.1029/2011MS000045.

Lawrence, P. J., et al. (2012), Simulating the biogeochemical and biogeophysical impacts of transient land cover change and wood harvest in the Community Climate System Model (CCSM4) from 1850 to 2100, *J. Clim.*, *25*, 3071–3095, doi:10.1175/JCLI-D-11-00256.1.

Le Quéré, C., et al. (2014), Global carbon budget 2013, *Earth Syst. Sci. Data*, *6*, 235–263, doi:10.5194/essd-6-235-2014.

Lewis, E., and D. Wallace (1998), *Program Developed for CO_2 System Calculations*, Carbon Dioxide Inf. Analy. Cent., Oak Ridge Natl. Lab., Oak Ridge, Tenn.

Lindsay, K., G. B. Bonan, S. C. Doney, F. M. Hoffman, D. M. Lawrence, M. C. Long, N. M. Mahowald, J. K. Moore, J. T. Randerson, and P. E. Thornton (2014), Preindustrial-control and twentieth-century carbon cycle experiments with the Earth system model CESM1(BGC), *J. Clim.*, *27*, 8981–9005, doi:10.1175/JCLI-D-12-00565.1.

Lovenduski, N. S., and T. Ito (2009), The future evolution of the Southern Ocean CO_2 sink, *J. Mar. Res.*, *67*, 597–617.

Maier-Reimer, E. (1993), Geochemical cycles in an ocean general circulation model. Preindustrial tracer distributions, *Global Biogeochem. Cycles*, *7*, 645–677.

Maier-Reimer, E., I. Kriest, J. Segschneider, and P. Wetzel (2005), *The HAMburg Ocean Carbon Cycle Model HAMOCC5.1—Technical Description Release 1.1, Berichte zur Erdsystemforschung 14*, 50 pp., Max Planck Institute for Meteorology, Hamburg, Germany.

Matthews, H. D., and K. Caldeira (2007), Transient climate-carbon cycle simulations of planetary geoengineering, *Proc. Natl. Acad. Sci. U.S.A.*, *104*, 9949–9954.

Matthews, H. D., L. Cao, and K. Caldeira (2009), Sensitivity of ocean acidification to geoengineered climate stabilization, *Geophys. Res. Lett.*, *36*, L10706, doi:10.1029/2009GL037488.

Mehrbach, C., C. H. Culberson, J. E. Hawley, and R. M. Pytkowicz (1973), Measurement of the apparent dissociation constants of carbonic acid in seawater at atmospheric pressure, *Limnol. Oceanogr.*, *18*, 897–907.

Meissner, K. J., T. Lippmann, and A. Sen Gupta (2012), Large-scale stress factor affecting coral reefs: Open ocean sea surface temperature and surface seawater aragonite saturation over the next 400 years, *Coral Reefs*, *31*(2), 309–319, doi:10.1007/s00338-011-0866-8.

Meinshausen, M., et al. (2011), The RCP greenhouse gas concentrations and their extensions from 1765 to 2300, *Clim. Change*, *109*, 213–241.

Mercado, L. M., N. Bellouin, S. Sitch, O. Boucher, C. Huntingford, M. Wild, and P. M. Cox (2009), Impact of changes in diffuse radiation on the global land carbon sink, *Nature*, *458*, 1014–1018, doi:10.1038/nature07949.

Muri, H., U. Niemeier, and J. E. Kristjánsson (2015), Tropical rainforest response to marine sky brightening climate engineering, *Geophys. Res. Lett.*, *42*, 2951–2960, doi:10.1002/2015GL063363.

Naik, V., D. J. Wuebbles, E. H. . Delucia, and J. A. Foley (2003), Influence of geoengineered climate on the terrestrial biosphere, *Environ. Manage.*, *32*, 373–381, doi:10.1007/s00267-003-2993-7.

Niemeier, U., H. Schmidt, and C. Timmreck (2011), The dependency of geoengineered sulfate aerosol on the emission strategy, *Atmos. Sci. Lett.*, *12*, 189–194, doi:10.1002/asl.304.

Niemeier, U., and C. Timmreck (2015), What is the limit of climate engineering by stratospheric injection of SO_2?, *Atmos. Chem. Phys.*, *15*, 9129–9141, doi:10.5194/acp-15-9129-2015.

Orr, J. C., et al. (2005), Anthropogenic ocean acidification over the twenty-first century and its impact on calcifying organisms, *Nature*, *437*, 681–686.

Phillips, O. L., et al. (2009), Drought sensitivity of the Amazon rainforest, *Science*, *323*(5919), 1344–1347, doi:10.1126/science.1164033.

Revelle, R., and H. Suess (1957), Carbon dioxide exchange between atmosphere and ocean and the question of an increase of atmospheric CO_2 during the past decades, *Tellus*, *9*, 17–27.

Robock, A., A. Marquardt, B. Kravitz, and G. Stenchikov (2009), Benefits, risks, and cost of stratospheric geoengineering, *Geophys. Res. Lett.*, *36*, L19703, doi:10.1029/2009GL039209.

Robock, A. (2013), The latest on volcanic eruptions and climate, *Eos Trans. AGU*, *94*(35), 305.

Robock, A. (2014), Stratospheric aerosol geoengineering, *Issues Environ. Sci. Tech.*, *38*, 162–185.

Rosenfield, J. E., D. B. Considine, P. E. Meade, J. T. Bacmeister, C. H. Jackman, and M. R. Schoeberl (1997), Stratospheric effects of Mount Pinatubo aerosol studied with a coupled two-dimensional model, *J. Geophys. Res.*, *102*(D3), 3649–3670.

Rozanov, E. V., M. E. Schlesinger, N. G. Andronova, F. Yang, S. L. Malyshev, V. A. Zubov, T. A. Egorova, and B. Li (2002), Climate/chemistry effects of the Pinatubo volcanic eruption simulated by the UIUC stratosphere/troposphere GCM with interactive photochemistry, *J. Geophys. Res.*, *107*(D21), 4594, doi:10.1029/2001JD000974.

Sakaguchi, K., X. Zeng, B. J. Christoffersen, N. Restrepo-Coupe, S. R. Saleska, and P. M. Brando (2011), Natural and drought scenarios in an east central Amazon forest: Fidelity of the Community Land Model 3.5 with three biogeochemical models, *J. Geophys. Res.*, *116*, G01029, doi:10.1029/2010JG001477.

Scott, V., S. Gilfilan, N. Markusson, H. Chalmers, and R. S. Haszeldine (2013), Last change for carbon capture and storage, *Nat. Clim. Change*, *3*, 105–111, doi:10.1038/nclimate1695.

Shepherd, J. G. (2012), Geoengineering the climate: An overview and update, *Philos. Trans. R. Soc. A*, *370*(1974), 4166–4175.

Six, K. D., and E. Maier-Reimer (1996), Effects of plankton dynamics on seasonal carbon fluxes in an ocean general circulation model, *Global Biogeochem. Cycles*, *19*(4), 559–583.

Steinacher, M., et al. (2010), Projected 21st century decrease in marine productivity: A multi-model analysis, *Biogeosciences*, *7*, 979–1005.

Stott, P. A., R. T. Sutton, and D. M. Smith (2008), Detection and attribution of Atlantic salinity changes, *Geophys. Res. Lett.*, *33*, L21702, doi:10.1029/2008GL035874.

Taylor, K. E., R. J. Stouffer, and G. A. Meehl (2012), An overview of CMIP5 and the experiment design, *Bull. Am. Meteorol. Soc.*, *93*, 495–498, doi:10.1175/BAMS-D-11-00094.1.

Thomas, R. Q., S. Zaehle, P. H. Templer, and C. L. Goodale (2013), Global patterns of nitrogen limitation: Confronting two global biogeochemical models with observations, *Global Change Biol.*, *19*, 2986–2998, doi:10.1111/gcb.12281.

Thornton, P. E., S. C. Doney, K. Lindsay, J. K. Moore, N. Mahowald, J. T. Randerson, I. Fung, J.-F. Lamarque, J. J. Feddema, and Y.-H. Lee (2009), Carbon-nitrogen interactions regulate climate-carbon cycle feedbacks: Results from an atmosphere-ocean general circulation model, *Biogeosciences*, *6*(10), 2099–2120, doi:10.5194/bg-6-2099-2009.

Thurber, A. R., A. K. Sweetman, B. A. Narayanaswamy, D. O. B. Jones, J. Ingels, and R. L. Hansman (2014), Ecosystem function and services provided by the deep sea, *Biogeosciences*, *11*, 3941–3963, doi:10.5194/bg-11-3941-2014.

Tilmes, S., M. J. Mills, U. Niemeier, H. Schmidt, A. Robock, B. Kravitz, J.-F. Lamarque, G. Pitari, and J. M. English (2015), A new Geoengineering Model Intercomparison Project (GeoMIP) experiment designed for climate and chemistry models, *Geosci. Model. Dev.*, *8*, 43–49, doi:10.5194/gmd-8-43-2015.

Tjiputra, J. F., K. Assmann, and C. Heinze (2010), Anthropogenic carbon dynamics in the changing ocean, *Ocean Sci.*, *6*, 605–614.

Tjiputra, J. F., C. Roelandt, M. Bentsen, D. M. Lawrence, T. Lorentzen, J. Schwinger, Ø. Seland, and C. Heinze (2013), Evaluation of the carbon cycle components in the Norwegian Earth System Model (NorESM), *Geosci. Model Dev.*, *6*, 301–325, doi:10.5194/gmd-6-301-2013.

Tjiputra, J. F., A. Olsen, L. Bopp, A. Lenton, B. Pfeil, T. Roy, J. Segschneider, I. Totterdell, and C. Heinze (2014), Long–term surface pCO_2 trends from observations and models, *Tellus B*, *66*, 23083, doi:10.3402/tellusb.v66.23083.

Volk, T., and M. I. Hoffert (1985), Ocean carbon pumps: Analysis of the relative strengths and efficiencies in ocean-driven atmospheric CO_2 changes, in *The Carbon Cycle and Atmospheric CO_2: Natural Variations Archean to Present*, edited by E. T. Sunquist and W. S. Broecker, pp. 99–110, AGU, Washington, D. C.